



Effects of Selective Laser Melting Process Parameters on Structural, Mechanical, Tribological and Corrosion Properties of CoCrFeMnNi High Entropy Alloy

Caner Bulut¹ · Fatih Yıldız² · Temel Varol^{3,4} · Gürkan Kaya² · Tevfik Oğuzhan Ergüder²

Received: 24 January 2024 / Accepted: 5 April 2024
© The Author(s) 2024

Abstract

The structural, tribological, mechanical, corrosion, and other properties of materials produced by laser-based powder bed fusion additive manufacturing methods are significantly affected by production parameters and strategies. Therefore, understanding and controlling the effects of the parameters used in the manufacturing process on the material properties is extremely important for determining optimum production conditions and for saving time and materials. This study aimed to determine the optimal laser parameter values for CoCrFeMnNi high-entropy alloy powders using the selective laser melting (SLM) method. The layer thickness was kept constant during experimentation. 5 different laser powers and 10 varying laser scanning speeds were tested, with hatch spacing from 30 to 90%. After determining the optimal laser parameters for SLM, prismatic samples were fabricated in different build orientations (0°, 45°, and 90°), and subsequently, their structural, mechanical, tribological, and corrosion properties were compared. Melt pool morphology could not be obtained at 20–40 and 60 W laser powers and at all laser scanning speeds used at these laser powers. At 100 W laser power, 600 mm/s laser scanning speed, and 70% hatch spacing parameters, an ultimate tensile stress of 550 MPa and elongation of 48% were obtained. Among the samples produced in different build orientations, the sample produced with a 0° build orientation exhibited the highest relative density (99.94%), the highest microhardness (201.2 HV_{0.1}), the lowest friction coefficient (0.7025), and the lowest wear and corrosion rates (0.7875 mpy). Additionally, SLM parameters were evaluated to have a significant impact on the performance of all properties of the samples.

Keywords High entropy alloys · Selective laser melting · Laser parameters · Structural properties · Wear · Corrosion

1 Introduction

The swift evolution of technology in modern times play an important role in the transformation of the manufacturing industry. It discusses the increasing importance of

enhancing the mechanical, corrosion, and tribological properties of materials due to the rapidly advancing technological developments in the manufacturing industry. In parallel with these and similar requirements developments, High Entropy Alloys (HEAs), which are among the new generation of material groups, attract the attention of researchers. The first scientific studies on the subject were published in 2004 by Yeh et al. [1] and Cantor et al. [2] started with the ideas of preparing equal or nearly equal multicomponent alloys [3]. HEAs usually contain 5–13 main elements, and the concentration of each element that makes up the alloy is between 5 and 35% [4–7]. HEAs, compared to traditional alloys, exhibit characteristics such as low and high temperature stability, machinability, corrosion resistance, high strength, and superior wear resistance [8, 9].

CoCrFeMnNi structure is one of the most studied HEA components in the literature [10]. This alloy has good mechanical properties and is known to offer high

✉ Caner Bulut
caner.bulut@igdir.edu.tr

¹ Technical Sciences Vocational School, Iğdır University, 76000 Iğdır, Turkey

² Department of Mechanical Engineering, Erzurum Technical University, 25100 Erzurum, Turkey

³ Department of Metallurgical and Materials Engineering, Karadeniz Technical University, 61080 Trabzon, Turkey

⁴ Medical Device Design and Production Application and Research Center, Karadeniz Technical University, 61080 Trabzon, Turkey

strength-ductility combinations, especially at cryogenic temperatures [11, 12]. Enhancing the properties of the production of this alloy is crucial to improving its usability in various applications. In this context, the selective laser melting (SLM) additive manufacturing method emerges as an important alternative to traditional manufacturing methods in the production of CoCrFeMnNi alloy, as evidenced by its use in various HEAs. SLM is a system based on the powder bed fusion (PBF) method and is among the important and widely used technologies in metal additive manufacturing [13, 14]. SLM is a new generation of additive manufacturing production technology in which a high-power laser melts and fuses the material powder laid on the production platform and can produce products with complex geometries [15, 16].

In order to obtain the targeted microstructure and mechanical properties, it is crucial to correctly select and optimize the laser production parameters/strategies and determine the most appropriate process conditions for a successful manufacturing process. Additionally, it is also important in terms of saving both material and time. The interaction of energy with the material, including energy absorption by the powder and melt pool, wetting of powder particles by the liquid, heat transfer within the powder, and the dynamics of the liquid pool, create complex connections in the control of this system. Additionally, the selection and optimization of processing parameters, including powder size, laser power, scanning speed, hatch spacing, scanning strategy, preheating temperatures, laser penetration depth, and layer thickness, directly impact the structural, mechanical, and surface properties of the produced parts [17–19]. In the SLM system, the presence of numerous parameters is in question; however, among these parameters, laser power (P), layer thickness (t), laser scanning speed (v), and hatch spacing (h) are commonly considered [20]. Laser energy density (E) is controlled by varying these four parameters [21]. The porosity, microstructure, and surface condition can be altered by changing sub-parameters while keeping the energy density constant [19, 22]. In order to ensure optimal manufacturing conditions, the influence of various process parameters, including layer thickness, hatch spacing, scan strategy, laser power, and scan speed, on the microstructure, mechanical properties, corrosion resistance as well as other properties such as density and surface quality, has been thoroughly investigated [23–26]. Very few studies have focused on the control of process optimization and the examination of melt pool behavior.

Zhang et al. [27] utilized different screening strategies to optimize the process parameters of CoCrFeNiMn HEA produced by SLM. They observed that increasing laser energy density initially led to higher sample density (up to 98.87%), but further energy increases resulted in decreased density, eventually stabilizing. Zhang et al. [28] examined

the influence of CoCrFeMnNi HEA on the formation and evolution mechanisms of cellular structures during LPBF. They observed that successive laser tracks applied multiple thermomechanical processes, resulting in an augmentation of dislocation density and cell thickness without compromising the cellular morphology or increasing misorientation of cell walls. Jia et al. [29] stated that the microstructure of the CoCrFeMnNi HEA samples they produced with SLM during the build phase consists of layer-by-layer overlapping melt pools, columnar grains, and cellular structures. They stated that the melt pool boundaries and cellular structures disappeared after the annealing process they applied to the samples, and they observed no significant compositional separation in the structure before and after annealing. Li et al. [30] observed that increasing laser energy density of the CoCrFeMnNi structure produced by SLM at different scanning speeds led to a higher density level and a better surface quality, but sample densities decreased at very high laser energy input. During the build process, it was stated that the Mn element exhibited a tendency to accumulate at the boundaries of the molten pool in comparison to other elements. They stated that the hot isostatic pressing (HIP) process applied to the samples improved both the density and mechanical properties, while also resulting in a more homogeneous distribution of Mn in the alloy. Piglione et al. [31] reported that CoCrFeMnNi HEAs produced via the SLM method display a microstructure characterized by rapid cooling, which induces the formation and epitaxial growth of fine grains within melt pools. Zhu et al. [32] stated that the melt pools of the high-density CoCrFeMnNi alloy produced by SLM exhibited a hierarchical structure, including columnar grains, sub-micron cellular structures, and dislocations, and reported that this phenomenon had a positive impact on the mechanical properties. Savinov and Shi [33] investigated the microstructural, mechanical, and corrosion behavior of samples produced by SLM at different scanning speeds. They reported that the heat-treated samples exhibited increased strength, enhanced ductility, and improved energy absorption. Additionally, they found that as the scanning speed decreased, pore density and size increased, while a higher laser scanning speed led to a decrease in corrosion resistance. Similar studies have been conducted on SLM-fabricated CoCrFeMnNi HEA in different scanning directions at a single energy density [26, 34–36]. The focus in the studies has been on microstructure and mechanical properties using fixed parameters with different scanning speeds and scanning directions.

Process parameters, temperature gradients and solidification variables in manufacturing with SLM are crucial in determining and optimizing the quality of the produced products, necessitating a comparative analysis of the melt pool to mitigate potential defects [37, 38]. Optimization studies for CoCrFeMnNi HEAs can further improve alloy

properties, guide different research, and expand their application areas. In addition to this, due to the high number of elements in HEA systems and the high cost and limited availability of the powders used, it can be estimated that they are relatively expensive compared to commercial alloys. This is also valid for powder bed additive manufacturing systems. In this research, systematic studies were carried out to minimize powder consumption, save time and reduce raw material costs by determining the optimum laser production parameters through parameter reduction. Moreover, parameters such as structural orientation, varying laser power, scanning speed, and hatch spacing have been insufficiently investigated systematically to determine their effects on the material performance of the CoCrFeMnNi alloy in the literature. In this study, variable structural orientations and different laser production parameters were employed during the fabrication of test samples, and their effects on microstructure, mechanical, tribological, and corrosion properties were investigated. It is believed that the parameters determined in our study will provide guidance for both different studies of the CoCrFeMnNi alloy and various research endeavors involving the addition of different elements to this alloy.

2 Experimental Details

In this study, the pre-alloy powders of CoCrFeMnNi, with a high purity of 99.9% by weight, were purchased from China by AddValue Additive Manufacturing Co. The particle size distribution of the equimolar CoCrFeMnNi alloy ranges from 10 to 50 μm , with an average size of approximately 25 μm . Upon examination of the SEM images, it was observed that the initial powders were predominantly spherical and did not display any agglomeration (Fig. 1). All samples were produced using the Concept Laser M Lab R (max. 100 W) device in continuous laser pulse mode within an Argon (Ar) gas atmosphere. During production, the oxygen concentration was kept below 0.2%. In the beginning, plates with a diameter of 15 mm were fabricated via the casting method from CoCrFeMnNi alloy powders for the application of single laser tracks. The single-tracks were applied to these cast specimens to examine the characteristics of the melting pools. The laser power ranged from 20 to 100 W in 20 W increments, while the scanning speed varied from 200 mm/s to 2000 mm/s in 200 mm/s increments. Subsequently, the specimens were cut at the center perpendicular to the laser

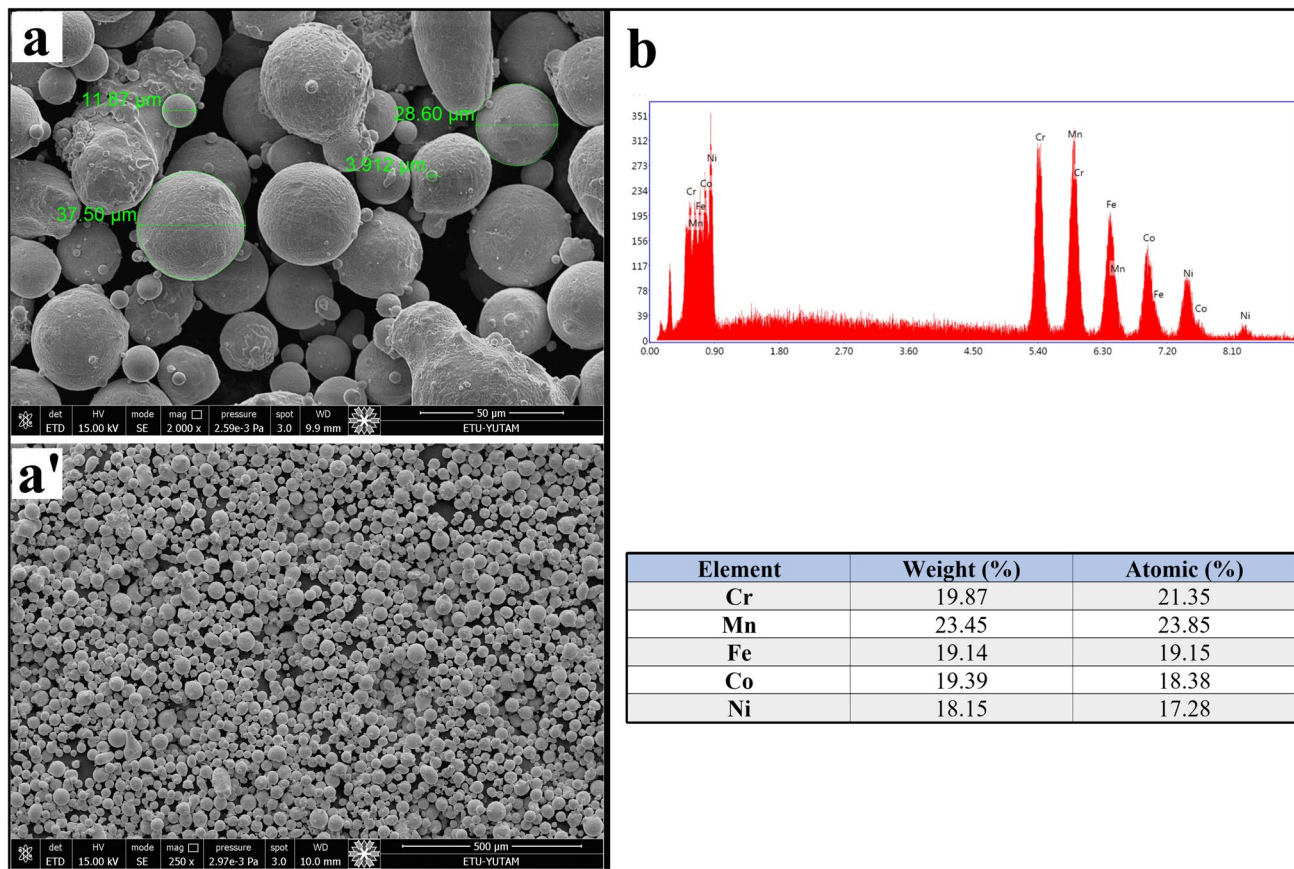


Fig. 1 CoCrFeMnNi HEA powders: **a–a'** SEM image, **b** EDS analysis

tracks, followed by cold molding. The specimens were sanded using 1500-grade SiC sandpaper and subsequently polished with diamond suspension. The surface characteristics of single-tracks and the geometries of melting pools on the CoCrFeMnNi plate were examined utilizing the Carl Zeiss-A1 optical microscope.

The tensile test specimen was dimensioned according to the ASTM E8 standard. Tensile tests were conducted employing the INSTRON-5982 tensile testing device, and all specimens were tested at ambient temperature with a constant tensile rate of 1 mm/min. The microstructure, wear, and corrosion test specimens were fabricated in prismatic form with dimensions of 10×10×5 mm using variable build orientations (0°–45°–90°).

The CoCrFeMnNi HEA powder's phases and the structures of specimens fabricated via SLM were determined employing Cu-K α radiation ($\lambda = 1.5405 \text{ \AA}$) with the GNR-Explorer X-ray diffractometer (XRD) device. Data was collected with a symmetrical scanning arrangement at an increment of 0.05° per second within the 30°–100° range. Subsequently, the XRD patterns were examined using the Match-software and their results were compared with existing literature.

The microstructure specimens were sanded using wet sandpaper in the range of 240–1500 numbers and polished with diamond suspension. Subsequently, the specimens were etched using a solution of HCl, HNO₃, and distilled water in a ratio of 1:1:1. Tribological examinations were conducted utilizing the Bruker-UMT tribometer testing device and performing three experiments for each specimen. Detailed tribological test parameters are presented in Table 1.

Morphological images of the CoCrFeMnNi powder material, worn surfaces, images of single-wall structures, fracture surfaces of tensile specimens, and microstructure images were acquired using the QUANTA-FEG 250 SEM device. The wear volumes and surface roughness of the specimens were assessed through the use of the Bruker-Contour GT 3D profilometer. To determine the occupancy rates, cross-sectional images captured with an optical microscope were processed using ZEISS ZEN 3.7 software, and

subsequent image analysis was conducted. Wear volumes were calculated by multiplying the wear trace area by its length. Microhardness measurements were conducted using the SHIMADZU HVM G-20 microhardness device. The measurements were conducted using the Vickers method, employing a 10-s dwell time and a 100 g load.

Corrosion tests were carried out at an ambient temperature of 25 °C in a 3.5% NaCl solution. The corrosion performance of all specimens was measured by potentiodynamic polarization. Corrosion specimens were prepared for testing after metallographic polishing. The corrosion properties of the specimens were measured with a Gamry Series G-750 potentiostat device, and the data analysis of the corrosion test results was evaluated with Gamry Echem Analyst software. To generate the polarization curves, a standard three-electrode system was performed at the electrochemical workstation equipped with a corrosion cell. In this direction, Ag/AgCl was used as a reference electrode (RE), HEA corrosion specimens as working electrodes, and graphite electrodes as counter electrodes (CE). During the test, the specimen surface was covered with insulating tape, and the surface area was reduced to 0.5 cm². To ensure a steady state potential, an open circuit potential (OCP) was measured over a duration of 5000 s. Potentiodynamic polarization curves were performed within the potential range of –600 to 600 mV, utilizing scan rates of 16.6 mV/s. All corrosion test measurements were repeated three times to determine the accuracy of the results.

3 Results and Discussion

3.1 Surface and Melting Pool Morphology of Single-Tracks

To assess the uniformity of laser tracks crucial for SLM production, single tracks were applied to CoCrFeMnNi plates. Optical microscope morphology images detailing the surfaces of these specimens are tabulated in Fig. 2, while cross-sectional images of the resulting melting pools are depicted in Fig. 3. The investigation underscored the significant influence of both laser power and scanning speed parameters on the formation of single tracks. Specifically, at low laser power and high scanning speeds, inadequate melting occurred, leading to the absence of discernible scanning tracks on the CoCrFeMnNi HEA plate's surface. This deficiency was especially pronounced after reaching a scanning speed of 1400 mm/s at a laser power of 20 W. Furthermore, even at different scanning speeds within this power range, achieving a consistent track proved elusive. Conversely, employing a laser power of 40 W revealed continuous tracks at a scanning speed of 1200 mm/s. However,

Table 1 Tribological test parameters

Test parameters	Values
Type	Reciprocating
Load (N)	3
Stroke (mm)	4
Velocity (mm/s)	8
Ball type	Al ₂ O ₃
Time (s)	3600
Temperature (C°)	(23 ± 2)
Ambient	Dry conditions

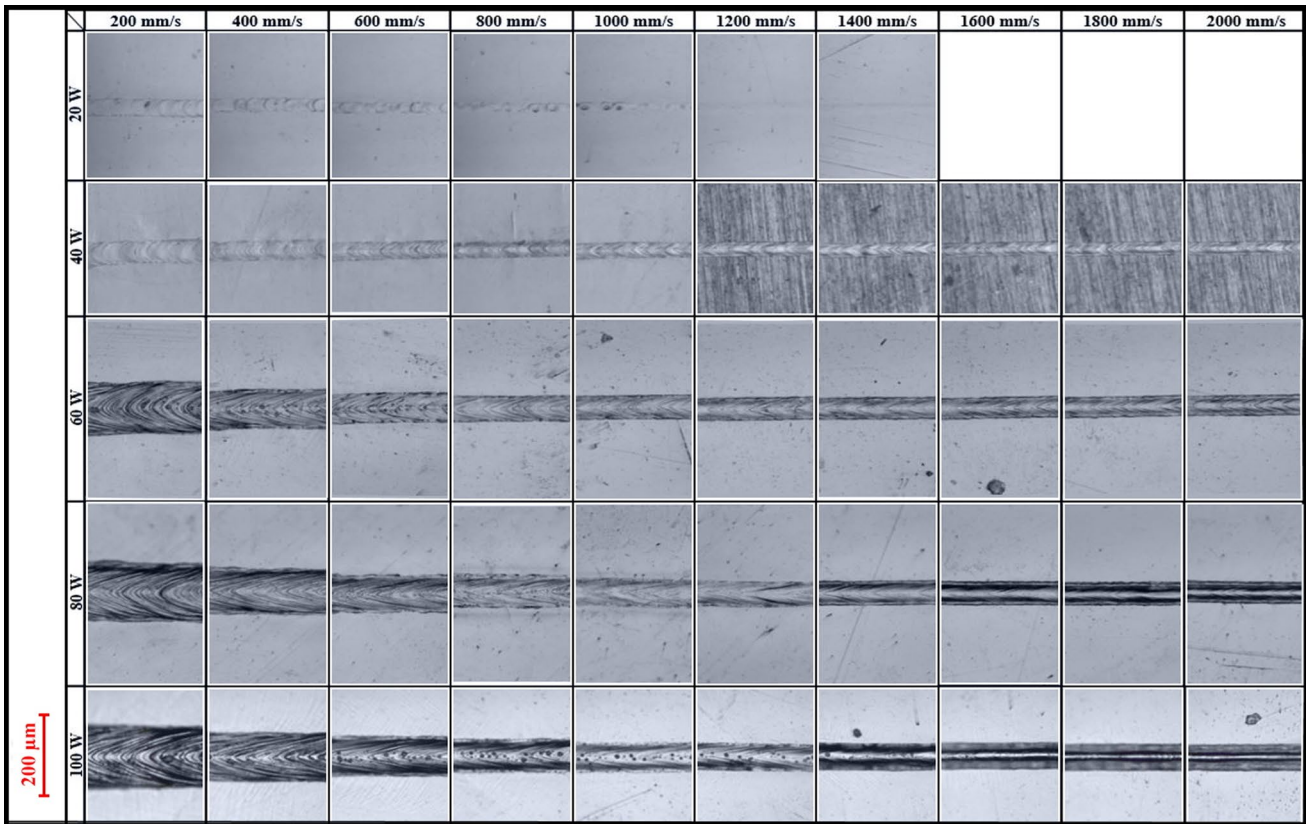


Fig. 2 Morphological images of surfaces resulting from single-tracks at different laser powers and scanning speeds

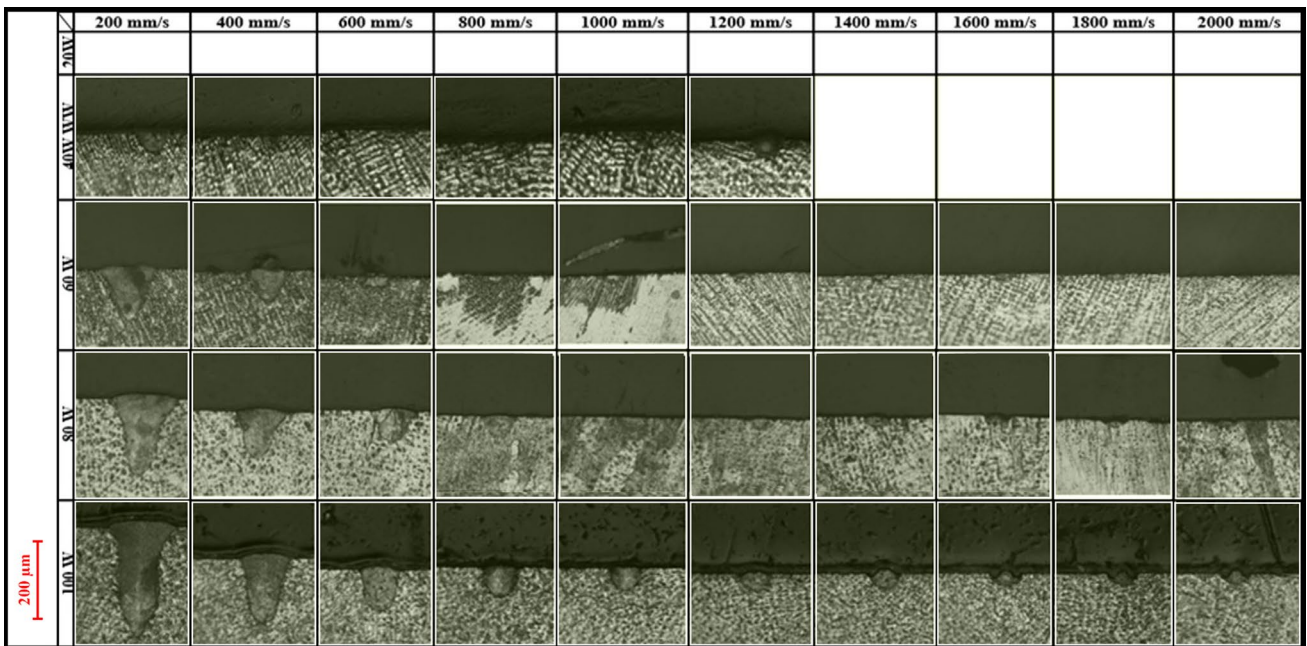


Fig. 3 Cross-sectional images of the melting pools resulting from single-tracks carried out at varying laser power and scanning speeds

instability within the track was observed, precluding the formation of a continuous melting line (Fig. 2).

After analyzing the cross-sectional images of the melting pools (Fig. 3), following the surface morphology findings, it became evident that insufficient heat generated by low laser power resulted in the absence of melting in the CoCr-FeMnNi plate, regardless of the scanning speed, after single tracks were executed with a 20 W laser power. Consequently, the specific characteristics of the melting pool could not be determined. Similarly, with a 40 W laser power, no melting was observed in the specimen at scanning speeds of 1400 mm/s, preventing the identification of the melting pool's features. However, at scanning speeds below this threshold, the melting pool became apparent, owing to its substantial depth. Melting pools were obtained more clearly due to the increased energy density due to increasing laser power and decreasing scanning speed values. Overall, an upward trend in both the width and depth of the molten pool was observed with the increase in laser power or the decrease in scanning speed.

As laser power increased and scanning speed decreased, the powder bed absorbed more energy, leading in an expanded width and depth of the melting pool. Upon examining the images of the melting pools, two distinct forms draw attention: one resembling a keyhole and the other an ellipse. The keyhole form occurs when the laser power is high and the laser scanning speed is small [39]. With increasing scanning speed values at the same power value, the melting pool form changes from keyhole to semi spherical form. Previous studies have reported the emergence of porous structures during the advanced stages of fabrication within keyhole mode melting pools [40]. Therefore, the parameters that yield the keyhole shaped melting pool form were not further examined in subsequent processes. Since penetration after single-tracks performed at 40 W and 60 W laser powers was minimal and production speed decreased at these power levels, focus shifted to processes performed at 80 W and 100 W laser powers.

Upon determining the melting pool forms, it was observed that collapse-like cavities formed in the upper corners of the melting pools obtained at high scanning speeds such as 1600, 1800 and 2000 mm/s (Fig. 4). This situation was

also observed in other melting pools formed after scanning at a speed of 1200 mm/s for 80 and 100 W laser powers. It is believed that this is due to the laser's inability to penetrate the relevant areas sufficiently at high scanning speeds. Therefore, single-wall structures were produced at different scanning speeds for 80 W and 100 W laser power.

3.2 Characterization of Single-Wall Structures Produced with the SLM

Following the analysis of melting pool forms, single-wall structures were produced at various scanning speeds, using 80 W and 100 W laser powers. The goal was to definitively determine the optimal values for laser power and scanning speed. To achieve this, $4 \times 5 \times 6$ mm geometries, as shown in Fig. 5, were produced using the SLM method. Single-wall structures were produced using scanning speeds of 800–1000–1200 mm/s at 80 W laser power and 600–800–1000 mm/s at 100 W laser power. These scanning speeds were chosen based on the parameters that yielded the semi-spherical form as the melting pool geometry.

SEM images depicting the single-wall structures are provided in Fig. 6 and 7. A thorough analysis of these SEM images revealed non-uniformity within the walls, with certain sections exhibiting irregularities as knots. Particularly, in productions carried out at 80 W laser power with scanning speeds between 1000 and 1200 mm/s, and at 100 W laser power with scanning speeds ranging from 800 to 1000 mm/s, these non-uniformities in the wall structures were evident. Conversely, in cases where production occurred at 80 W laser power with a scanning speed of 800 mm/s and 100 W laser power with a scanning speed of 600 mm/s, the single-wall structures displayed a remarkable level of uniformity. These structures exhibited a notably denser structure compared to those obtained at other scanning speeds. Upon comprehensive assessment of these findings, it was determined that the optimum production parameters were 80 W laser power with an 800 mm/s scanning speed and 100 W laser power with a 600 mm/s scanning speed. These parameters were ascertained while maintaining a constant layer thickness of 25 μ m.

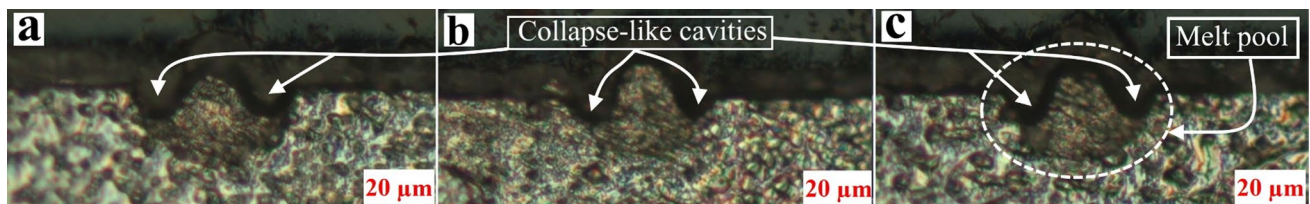


Fig. 4 Melting pool images of single-tracks performed at 100 W laser power and different laser scanning speeds; **a** 1600 mm/s, **b** 1800 mm/s and **c** 2000 mm/s

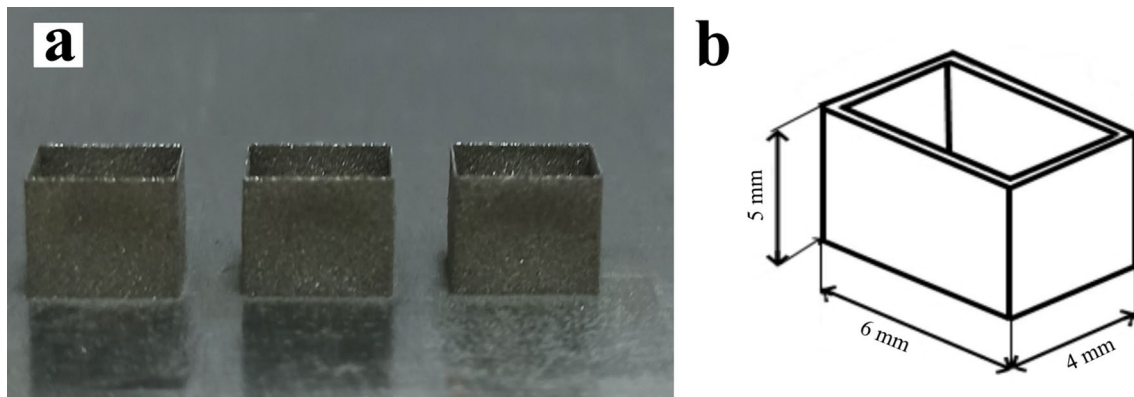


Fig. 5 Single-wall structures; **a** their appearances on the build platform, **b** technical drawing image

3.3 Optimization of Hatch Spacing Parameter

As part of this investigation aimed at optimizing SLM production parameters through a systematic reduction of variables, the quest for the optimum hatch spacing was initiated. This step followed the determination of laser power and laser scanning speed parameters.

To examine the hatch spacings to be tested in production with SLM, the wall thickness values of the single-wall structures produced with 80 W laser power at a scanning speed of 800 mm/s and 100 W laser power at a scanning speed of 600 mm/s were determined as 83.10 μm and 106.8 μm , respectively (Fig. 6a and Fig. 7a). It's worth noting that the hatch spacing (hs) value was expressed as a percentage of the wall thickness (WT) value in this study.

3.3.1 Relative Density Measurements

To investigate the influence of hatch spacing on relative density, cylindrical specimens measuring 6 mm in diameter and 4 mm in height were manufactured at various hatch spacings. This was achieved using an 80 W laser power with an 800 mm/s scanning speed and a 100 W laser power with a 600 mm/s scanning speed. In order to reduce powder material consumption, cylindrical specimens were initially produced with a 10% increment in hatch spacing, ranging from 30 to 90% of the determined wall thickness values, before manufacturing tensile specimens.

The optical microscope images used to evaluate the relative densities of the hatch spacing specimens produced with the 80 W-800 mm/s and 100 W-600 mm/s parameters are shown in Fig. 8 and the graphical distribution of the relative densities is shown in Fig. 9. Table 2 shows the numerical values of the relative densities of the specimens produced with different hatch spacings. When Fig. 8 was examined, it was seen that cavities formed within the structure due to excessive heat input at hatch spacing values 30hs, 40hs and

50hs obtained with both laser powers. Although high relative densities (over 99%) were achieved for the 80hs and 90hs hatch spacings with both laser powers, a breaking point occurred due to insufficient overlap of laser tracks, resulting in a decrease in relative densities. The relative density of the specimens produced at 70hs was higher than the other specimens for both laser powers. Therefore, at this stage, the optimum value was determined to be a 70% hatch spacing, where the highest relative densities were obtained. Mechanical tests were subsequently conducted by producing tensile test specimens at these parameters.

3.3.2 Mechanical Properties

To investigate the mechanical properties, tensile specimens were vertically fabricated at parameter values of 80 W-800 mm/s and 100 W-600 mm/s, utilizing a 70% hatch spacing, which provides the most favorable results in terms of relative densities (Fig. 10a). Images of the samples after testing are presented in Fig. 10a'. According to the results, the optimum production parameter set for the SLM method was determined based on the performance criteria of the highest density rate and elongation.

Upon analysis of the tensile curves, the elongations of the specimens produced at 80 W-800 mm/s and 100 W-600 mm/s, with a 70% hatch spacing, were measured at 25% and 48%, respectively (Fig. 10b). No notable difference was observed among the specimens in terms of tensile stresses, with values of approximately 560 MPa for 80 W and 548 MPa for 100 W. The main reason for this results is that the specimens produced at 100 W-600 mm/s parameters also exhibit the highest relative density. Metallurgical defects, such as pores and cracks, within the structures of materials fabricated through SLM lead to a reduction in mechanical properties [30]. Additionally, it is known in the scientific literature that applied SLM parameters (e.g., laser

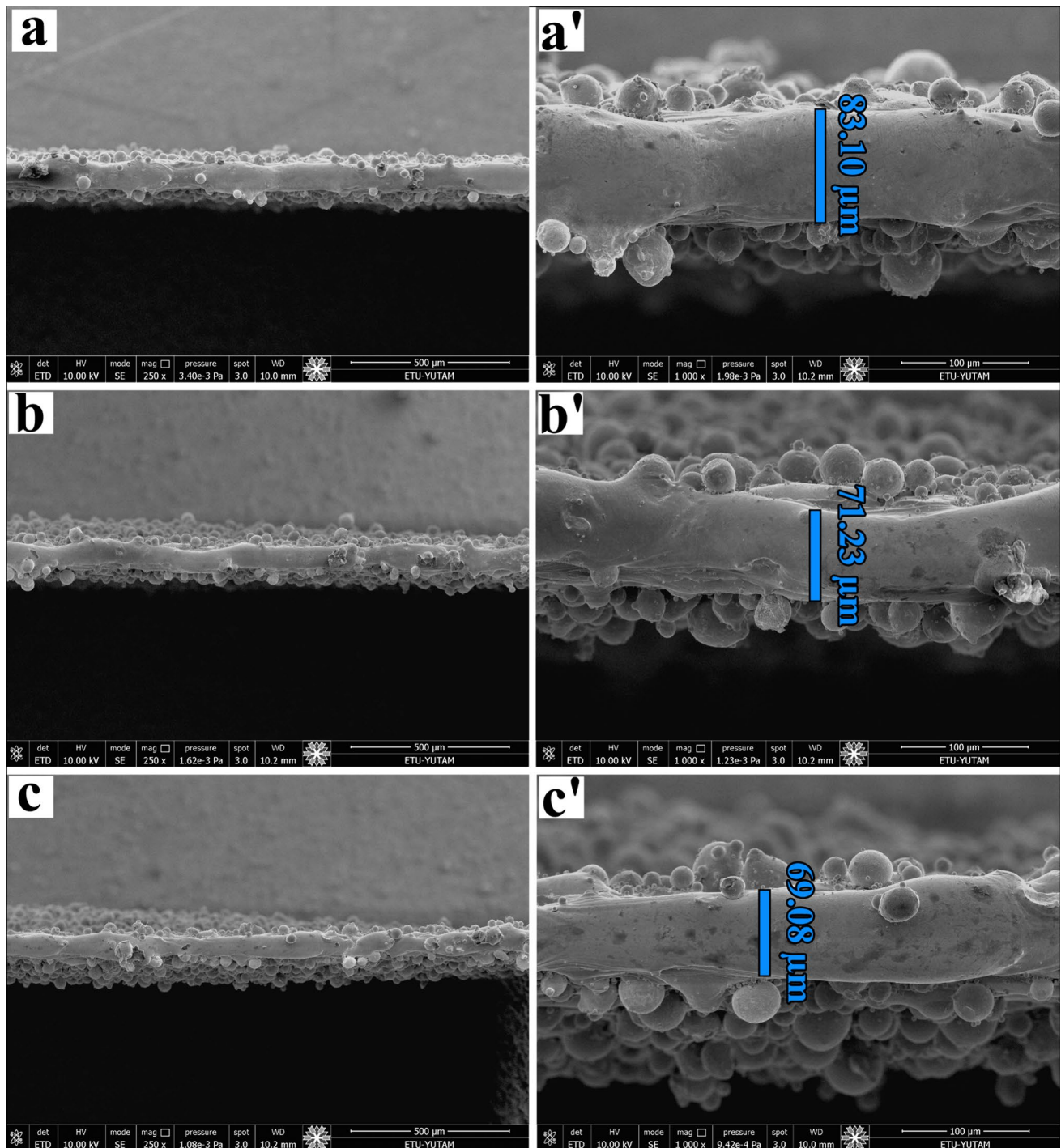


Fig. 6 SEM images of single-wall structures, **a–a'** 80W-800 mm/s, **b–b'** 80W-1000 mm/s, **c–c'** 80W-1200 mm/s

power, scanning speed, etc.) affect the density and mechanical properties of the material [32, 41].

A widely accepted fundamental limitation in the SLM production process is the insufficient bonding between layers and the insufficient elongation caused by the microstructure resulting from rapid cooling [42]. Given the absence of a significant difference in the tensile strengths of the

specimens produced using two different parameter sets, the elongation at the moment of fracture has been adopted as the criterion regarding mechanical properties within the scope of this study. At this stage, a higher elongation was obtained compared to the literature data, with an elongation of 48% achieved from the tensile specimens produced using the parameters 100 W-600 mm/s.

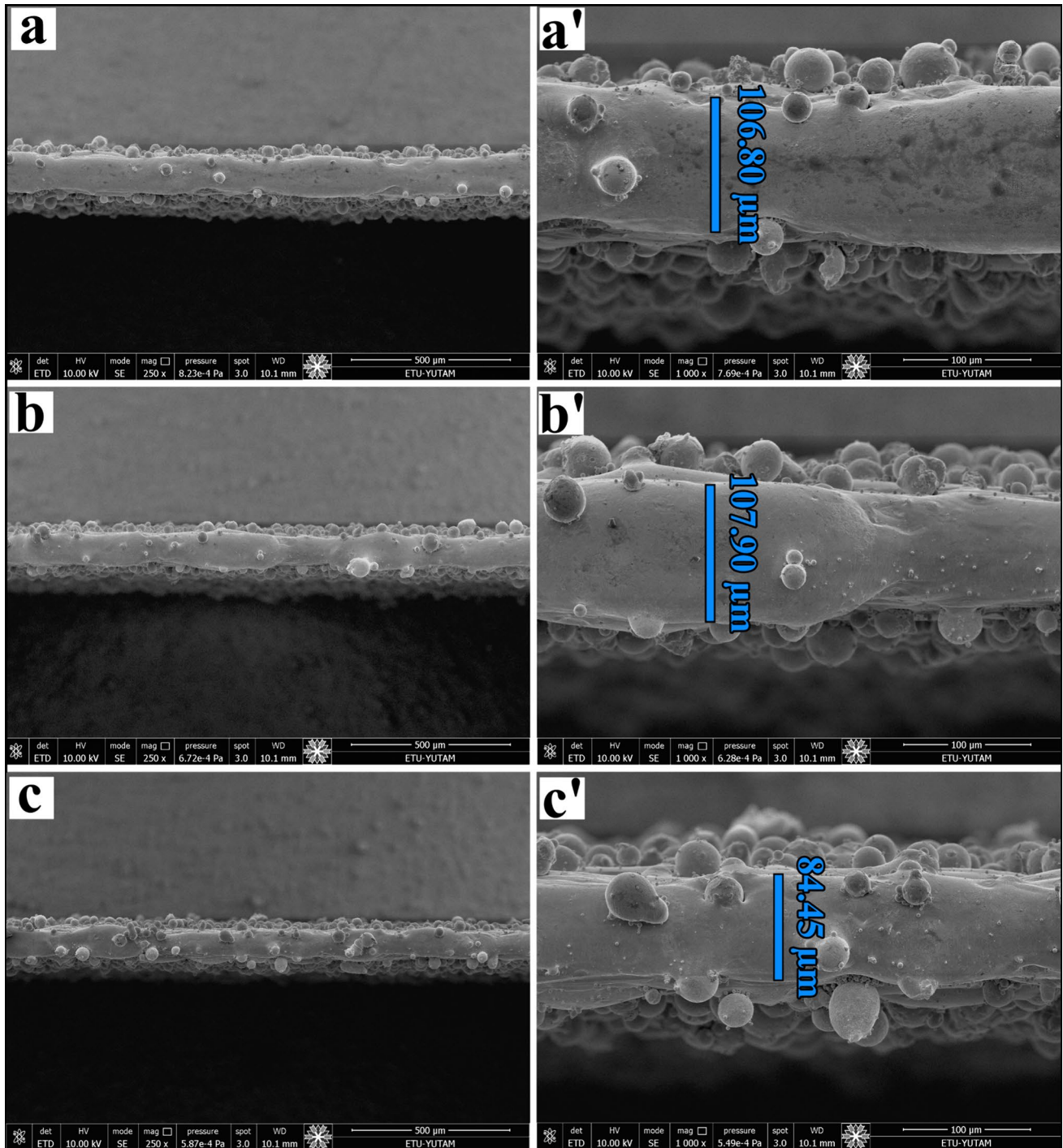


Fig. 7 SEM images of single-wall structures **a–a'** 100W-600 mm/s, **b–b'** 100W-800 mm/s, **c–c'** 100W-1000 mm/s

Figure 11 shows SEM images of the fracture surfaces of tensile samples. The fracture surfaces of the samples produced with both laser powers exhibit the presence of equiaxed pits, a spongy structure on the surfaces, and ductile fracture characterized by a cone-bowl fracture mode. This damage mechanism observed in the sample leads to fracture through the formation and coalescence of micro-voids,

resulting in the characteristic appearance of the fracture surface [43, 44]. It has been reported that as the average grain size increases, the size of the pits in the structure also increases, leading to a lower amount of active micro voids and deeper pits [45]. The presence of these deep pits on the surface, attributed to the delayed coalescence of micro-voids depending on grain size, is consistent with ductile fracture

Fig. 8 The images of hatch spacing specimens produced with 80 W-800 mm/s and 100 W-600 mm/s

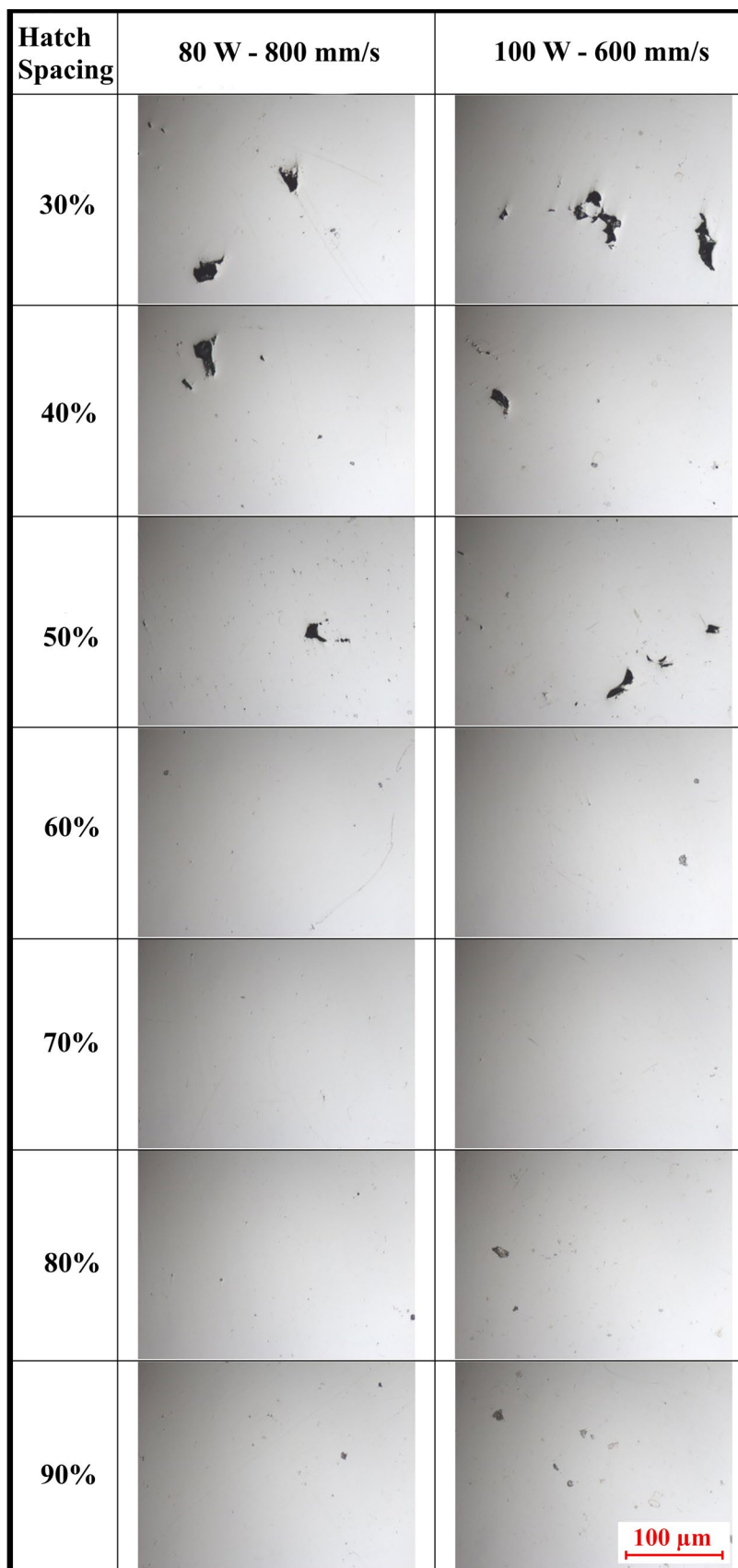
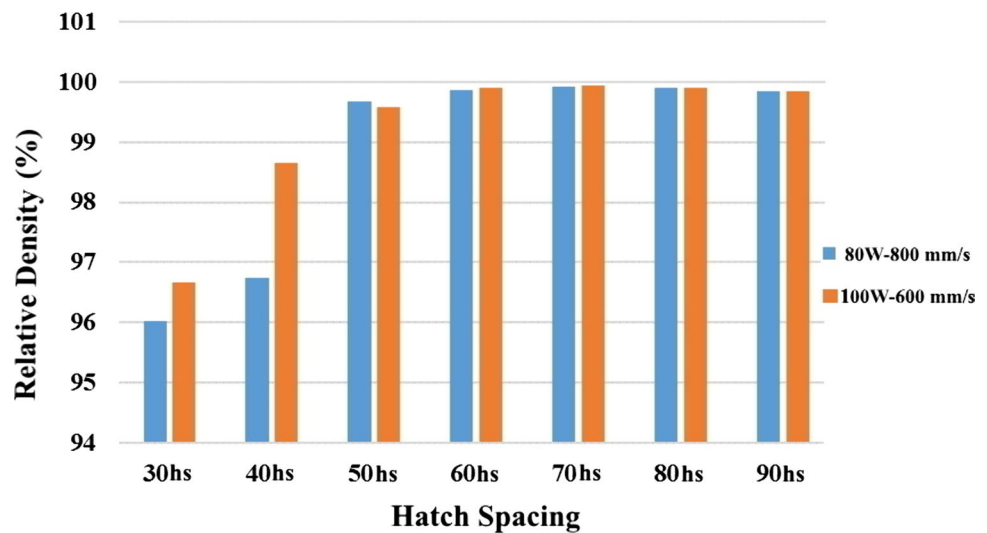


Fig. 9 Graphical distribution of the relative densities of the specimens



behavior as indicated by the stress–strain curve. Samples produced under 100W-600 mm/s parameters have exhibited a more pronounced display of ductile fracture mode. Micro-particles were observed within the micro-pits formed in the samples produced under the 80W-800 mm/s parameters. In addition to the quantity of voids within the structure, the widespread presence of these micro-particles may contribute to the premature fracture of the material during tensile testing.

Table 3 presents the optimal production parameter set for the SLM process based on the obtained results, where the highest values of relative density and elongation are considered as performance criteria.

3.4 Structural Properties of the Specimens Produced Using Different Build Orientations

With the optimum SLM parameters presented in Table 3, microstructure and relative density specimens of CoCrFeMnNi HEA were fabricated in prismatic form using different build orientations (0° – 45° – 90°) with dimensions of

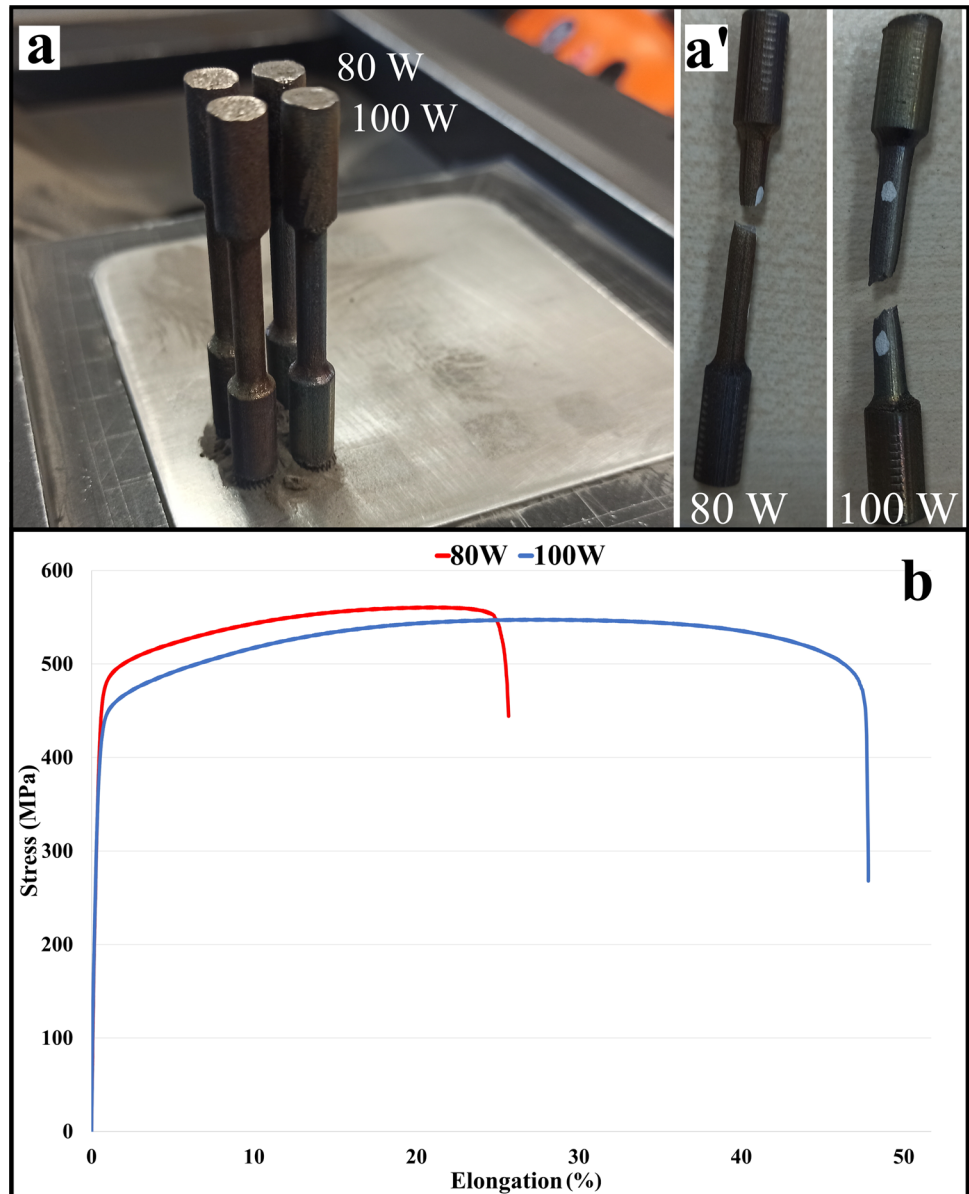
$10 \times 10 \times 5$ mm (Fig. 12). In this section, the effects of different build orientations on the relative density and microstructural properties are investigated.

SEM microstructural images captured from the surfaces of the prismatic test specimens, fabricated via the SLM method in three distinct build orientations employing the optimum parameter set, are presented in Fig. 13. Two types of microstructures are observed in the structure of melt pools. These microstructure images reveal a fine cellular structure and some grains exhibit dendritic growth, making the microstructure more uniform than other orientations. This microstructure emerged as a consequence of rapid solidification, attributed to the elevated cooling rates inherent to the SLM process. This situation mirrors the structures achieved through the casting process [46]. The development of cellular or dendritic grains relies on the temperature gradient (G) and solidification rate (R). When the temperature field G is low and R is high, it causes the formation of equiaxed or cellular grains, and when the opposite situation occurs (i.e., G is high and R is low), it causes the formation of dendrite columnar grains [47]. This case was elaborated on and reported in detail by Song et al. [48]. In addition, high energy density can lead to directional heat transfer and resulting directional solidification [49]. Samples produced with 0° building orientation have a predominantly cellular microstructure, and the structure of the layers cannot be observed since the surface perpendicular to the building direction is examined (Fig. 13a). In the border regions of cellular structures, dendritic structures are more apparent. The formation of cellular and columnar structures in the CoCrFeNiMn alloy produced by SLM has been reported [30–32]. However, as the build orientation angle increased, it was observed that the grains within the microstructure of the specimens created with a 45° build orientation began to exhibit a preferential growth (Fig. 13b). The flows occurred

Table 2 Relative densities of the specimens

Name of specimens	80 W – 800 mm/s	100 W – 600 mm/s
	Relative density (%)	
30 hs	96.01	96.67
40 hs	96.74	98.66
50 hs	99.68	99.59
60 hs	99.86	99.90
70 hs	99.91	99.94
80 hs	99.91	99.89
90 hs	99.84	99.84

Fig. 10 **a** Images of tensile test specimens on the build platform, **a'** images of specimens after the test, **b** Tensile test results of the specimens produced with 80 W–800 mm/s and 100 W–600 mm/s at 70% hatch spacing



at the boundaries of the voids in this sample due to the influence of heat input. This situation can be attributed to the increased presence of pores and the build orientation. Since the surface parallel to the build direction was analyzed in Fig. 13c, the horizontal lines of the layer structure became more evident. Dendritic growth appears to be concentrated in the microstructure of this sample. Additionally, there are pores in some places on all sample surfaces. Figure 14 shows the optical microscope images of the samples. After the etching process, grain structures can be observed more clearly according to the building orientation with optical images taken from the sample surfaces. In addition, structural defects such as voids and pores in the structures can be observed more clearly, supporting Fig. 13. As a result, apart from rapid solidification, the scanning strategy may

influence the directionality of solidification. Therefore, it may have an impact on the formation of the microstructure.

The XRD results for the CoCrFeMnNi HEA specimens, produced through the SLM method with different build orientations, are presented in Fig. 15. FCC structure peaks were obtained for the (111), (200), (220), (311), and (222) planes of all CoCrFeMnNi HEA specimens produced at various build orientations. The planes obtained with all build orientations were in agreement with other literature studies for the CoCrFeMnNi structure [28, 29, 50]. There was no phase change in the CoCrFeMnNi alloy produced at various build orientations only the FCC phase structure was observed. No significant shift in the peak positions of the analyzed specimens was observed, but different intensity values were obtained. The reason for this situation is

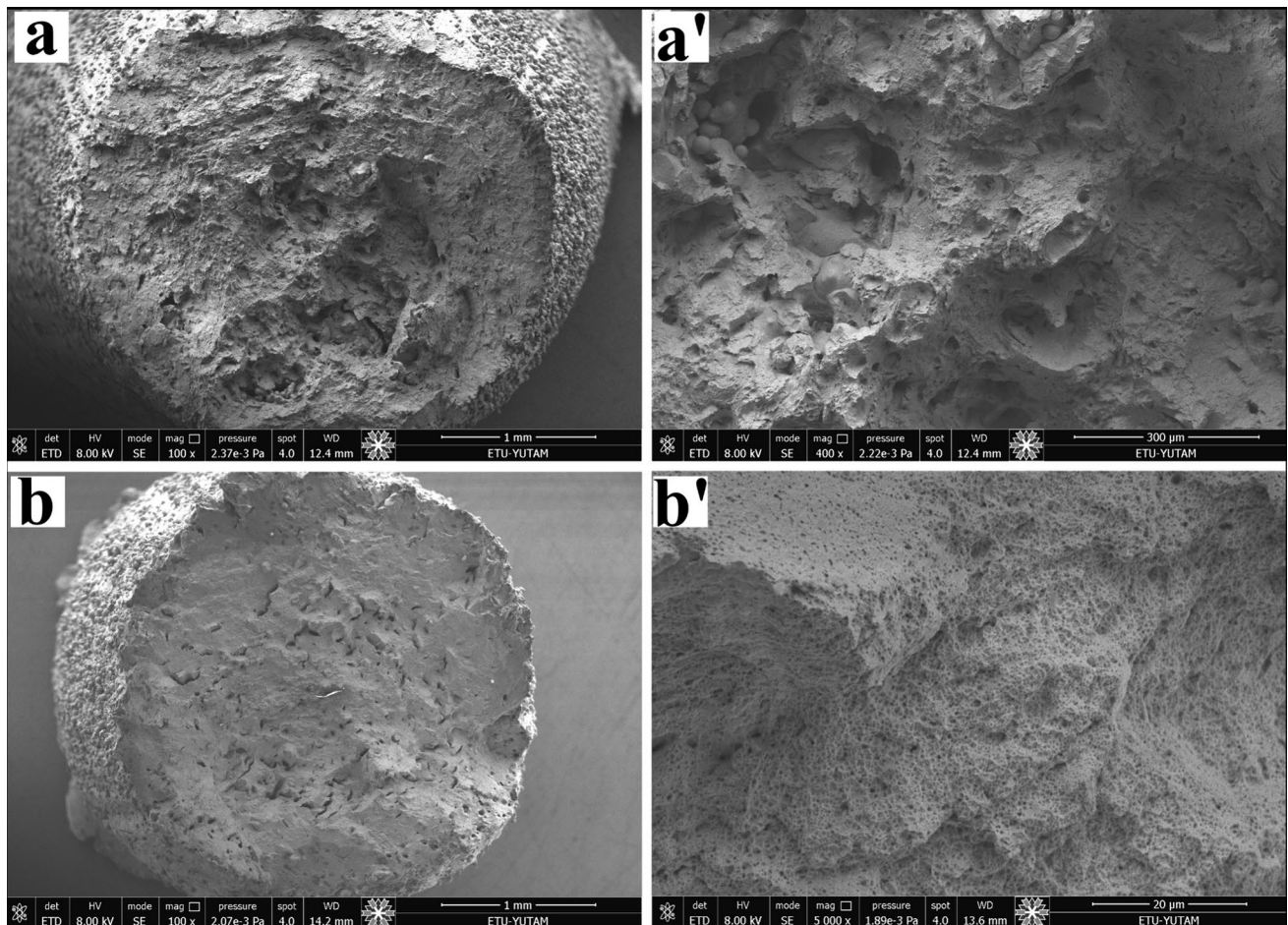


Fig. 11 SEM images of the fracture surface of tensile specimens produced with a hatch spacing of 70%; **a–a'** 80 W-800 mm/s, **b–b'** 100 W-600 mm/s

Table 3 Optimum production parameter set

Laser power (W)	Scanning speed (mm/s)	Hatch spacing (% WT)	Layer thickness (μm)
100	600	70	25

the texture change in the structure after different build orientations are used in production. In addition, the change in peak intensities indicated the presence of residual stresses that cause lattice distortions.

The selection of suitable process parameters greatly influences the porosity or density of materials fabricated through SLM. In addition to parameter selection, the solidification rate of the material plays a crucial role in the SLM process. Excessively high energy density can lead to heightened porosity attributed to phenomena such as keyhole formation, spattering, and other adverse effects, resulting in the entrapment of gas within the melt [51].

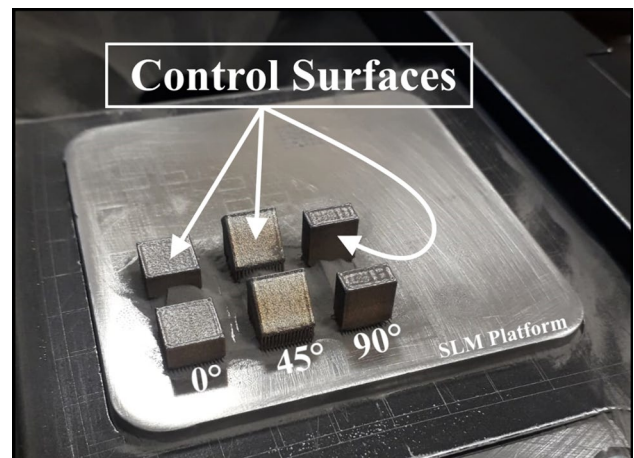


Fig. 12 Views of CoCrFeMnNi specimens produced at different build orientations (0°–45°–90°) on the SLM platform

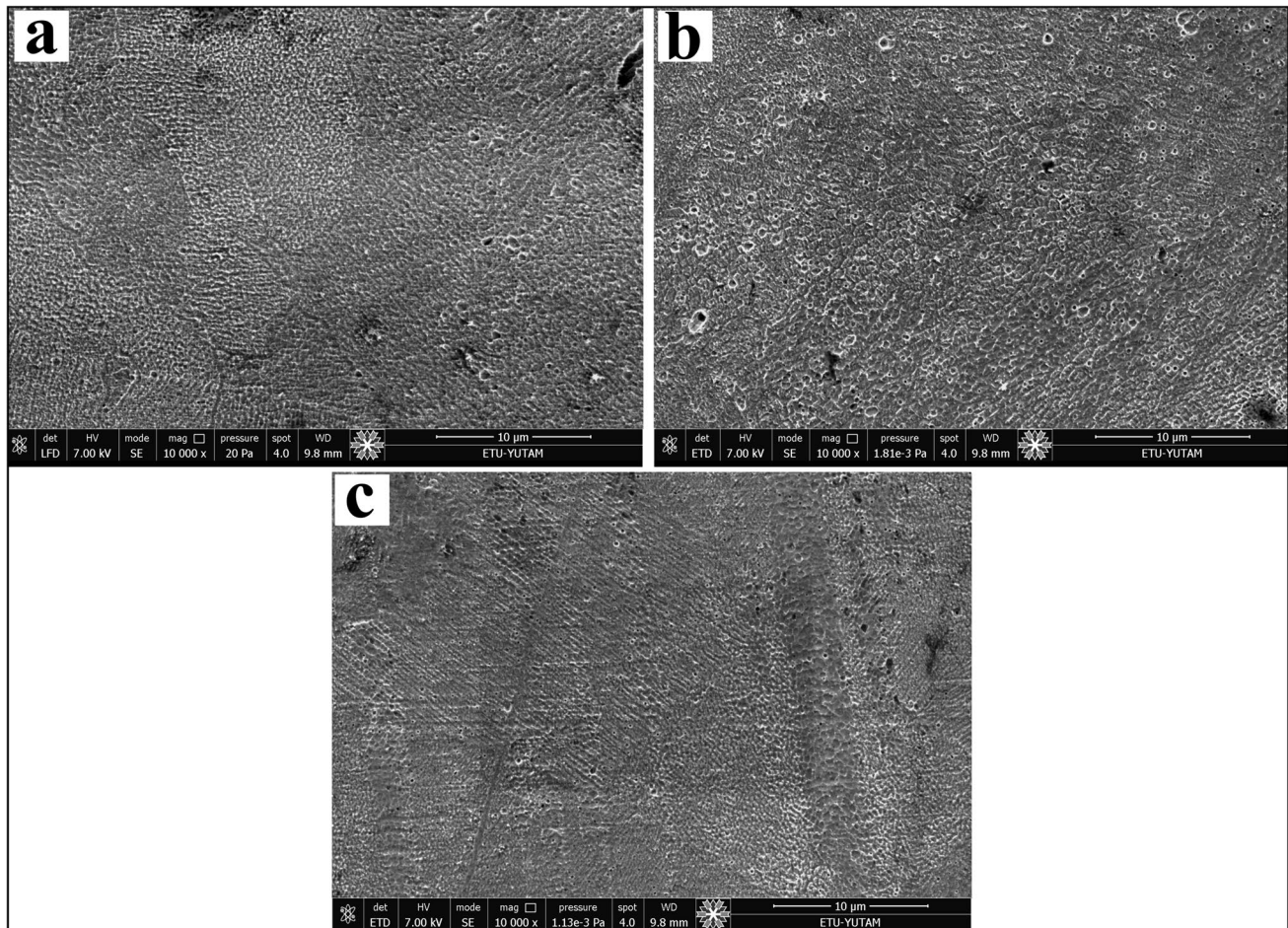


Fig. 13 Microstructure SEM images of CoCrFeMnNi HEA specimens produced at different build orientations with the optimum parameter set; **a** 0°, **b** 45° and **c** 90°

Relative densities of prismatic test samples produced in different directions using the optimum parameter set were image analyzed using an optical microscope (OM). The results of density measurements are presented in Fig. 16 and Table 4. According to the results, it was observed that the build orientation had an effect on the relative density, and values above 99% were obtained in all three build orientations. In the three build orientations, high-density specimens were obtained with volumetrically uniform layers. The sample produced with a 45° orientation exhibited the highest porosity rate at 0.33%, whereas the sample produced with a 0° orientation demonstrated the lowest porosity rate at 0.06%. A significant difference in relative densities between structure orientations at 45° and 90° was not observed. However, since the layers in the sample produced with a 45° orientation overlap in a staircase shape, it is expected to have more pore structure than other samples. Apart from the density data, Fig. 13b also supports this situation. A relative density exceeding 99% was achieved with the VED input of 89.17 J/mm³ and its effect on the alloy samples.

These results clearly demonstrate that the SLM parameters utilized for HEA production are highly suitable in terms of relative densities.

3.5 Characterization of Tribological Properties of CoCrFeMnNi Specimens Produced Using Different Build Orientations

Tribological tests were conducted on specimens produced in three different build orientations, utilizing the optimal parameter set outlined in Table 3. The control surfaces, as depicted in Fig. 12, underwent wear tests using the parameters specified in Table 1. Additionally, microhardness measurements were obtained from the polished control surfaces. Before starting tribological tests, the surface roughness (Ra) of the samples was directly evaluated immediately after SLM fabrication. The measurements were taken at three different points from all specimens produced at various build orientations. Surface roughnesses were measured as 2.17 µm, 2.33 µm and 2.36 µm for specimens produced in

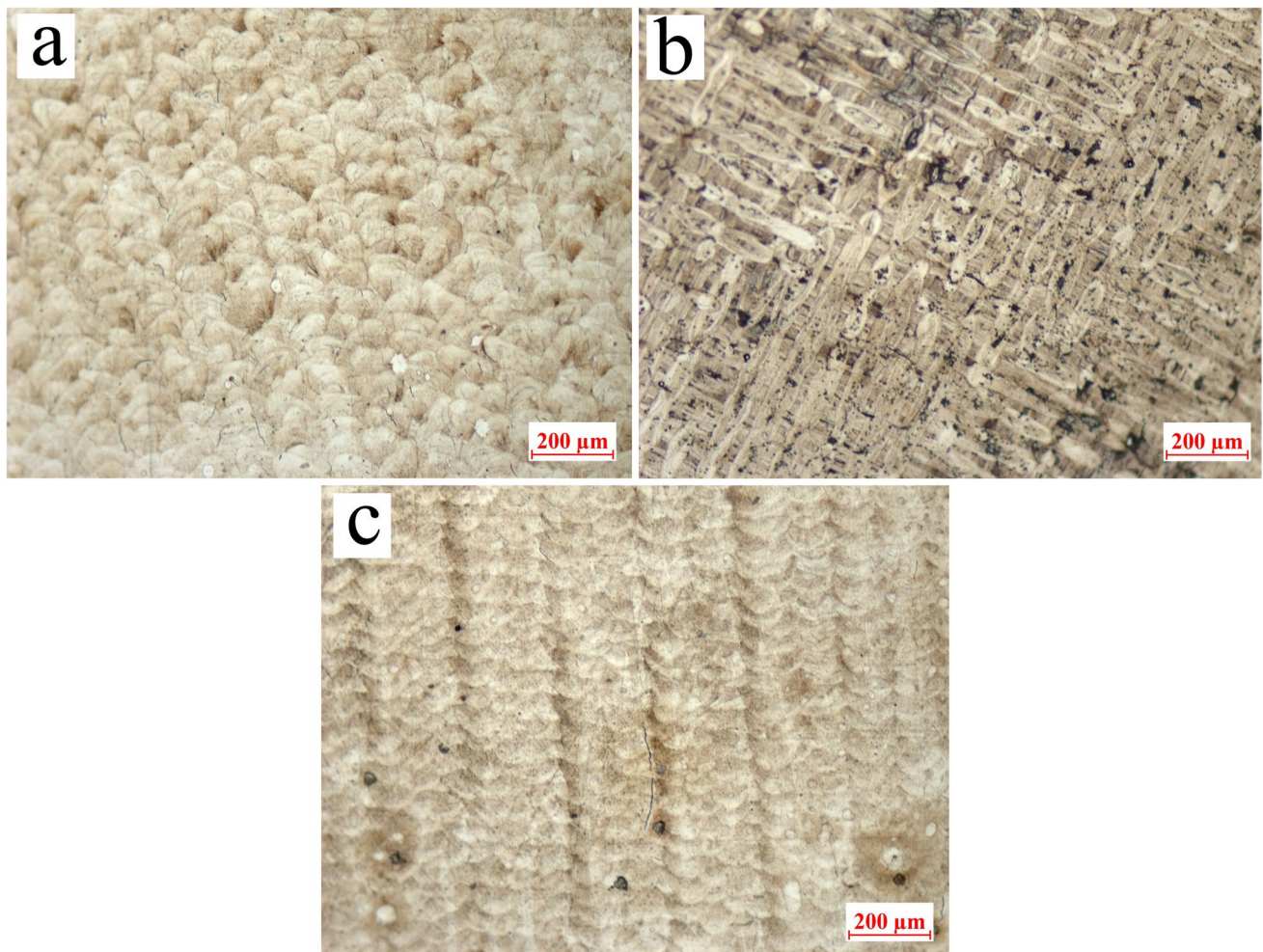


Fig. 14 OM images of samples produced in different structural directions with the optimum parameter set: **a** 0°, **b** 45°, and **c** 90°

0°, 45° and 90° build orientations, respectively. Subsequent to the application of metallographic procedures, the average surface roughnesses for all specimens were reduced to an average of 0.05 μm .

The friction coefficient (COF) is an important parameter used to analyze friction and wear performance. Generally, a lower COF under ideal wear conditions indicates superior wear behavior of the material [52]. Figure 17 shows the sliding time curves of the COF coefficients for samples produced with three different build orientations (0°–45°–90°) using the optimum parameter set. The COF values for all samples exhibited a sharp increase following an initial bedding-in period after the initial contact at the onset of the wear test. The friction coefficient of all three samples reached the steady-state period in a very short time and stabilized in the later stages of the test. It was noteworthy that the resulting friction coefficient curves for all specimens closely paralleled each other. The similarity in the running-in period for all three samples is attributed to the close surface profiles of the specimens and the smoothness of the surfaces due to

pre-wear-test metallographic treatments. The average COF values for the specimens were summarized in Table 5. The 90° build sample exhibited the highest average COF with a value of 0.8035, while the average COF values for the 45° and 0° build samples decreased to 0.7717 and 0.7205, respectively. The reduction in the contact area between the counter ball and the surface during sliding wear has been reported to lead to a decrease in the coefficients of friction as a result [53].

During the wear test, the fluctuation in the curve occurring between 1200 and 1800s of the sample produced with a 0° construction orientation differed compared to other samples. Other samples exhibited a similar situation throughout the entire test period. An oxidation reaction occurs under the influence of the applied load and shear rate during the test. The occurrence stems from elevated frictional heat at the interface due to ambient conditions (air atmosphere and abrasive Al_2O_3 ball), resulting in the formation of oxides and oxide films. Oxides formed on the sliding surface due to frictional heat act as a barrier to ball

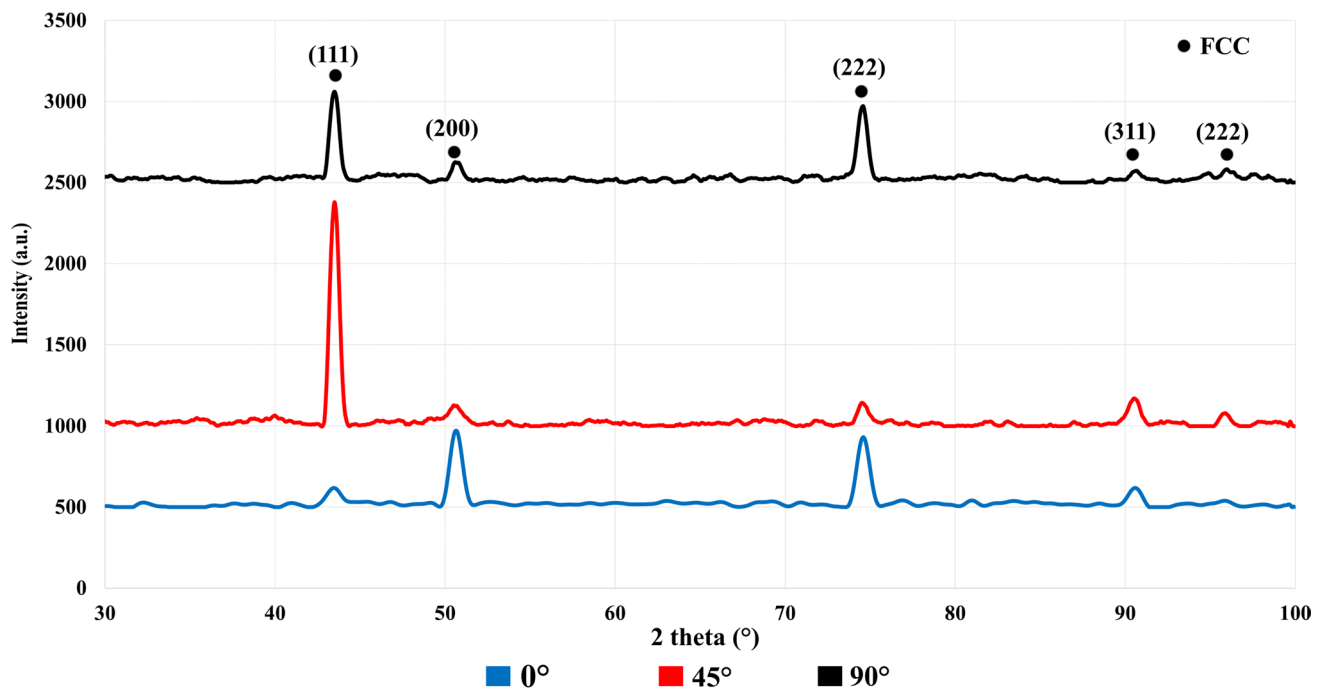


Fig. 15 XRD graph of CoCrFeMnNi HEA specimens produced at various build orientations

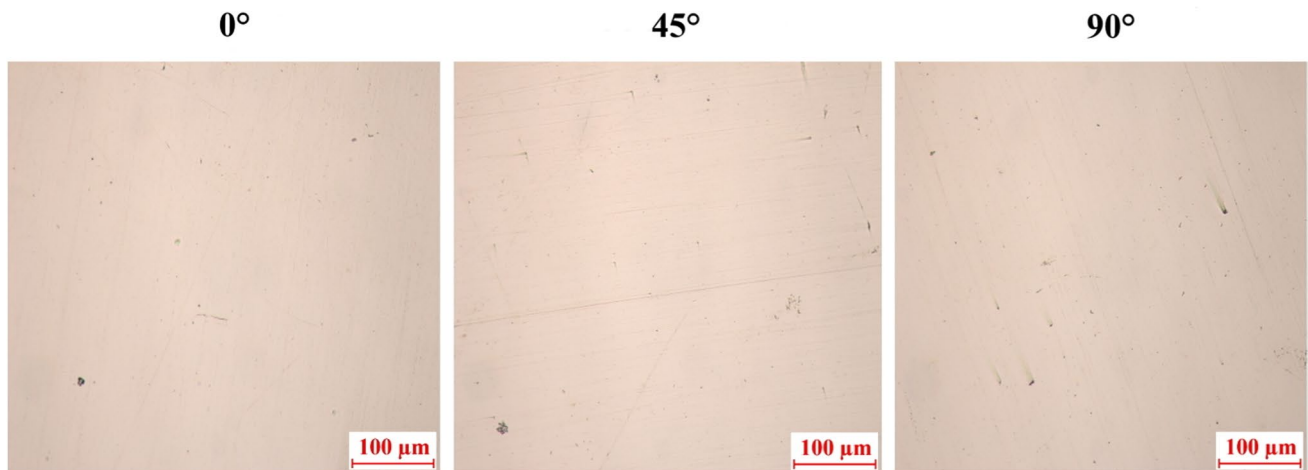


Fig. 16 Optical microscope image of CoCrFeMnNi specimens produced at different build orientations

Table 4 Relative densities of specimens produced using different build orientations

Composition/alloy (HEA)	Build orientation	Relative density
CoCrFeMnNi	0°	99.94
	45°	99.67
	90°	99.74

movement and can cause the curves to fluctuate more. This state may also result in plastic deformation of the material. Hence, it is hypothesized that the alterations in the fluctuations noted between 1200 and 1800s in the sample fabricated with a 0° building orientation stem from this situation. As the test progresses, numerous oxides accumulate to form a continuous oxide layer, which serves as

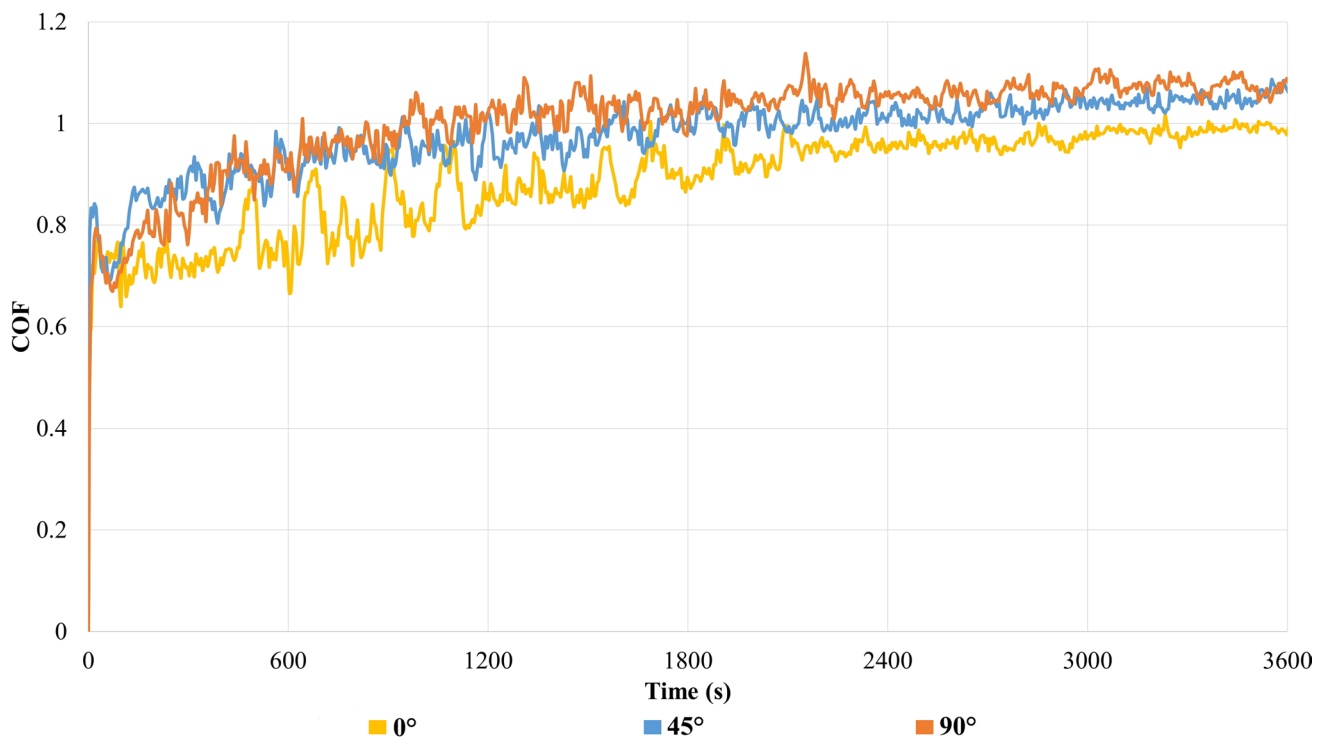


Fig. 17 Friction coefficient-time plot of CoCrFeMnNi specimens produced at different build orientations

Table 5 Average coefficient of friction values of CoCrFeMnNi HEA specimens produced at 0°, 45° and 90° build orientations

Composition/ally (HEA)	Build orientation	Average coefficient of friction
CoCrFeMnNi	0°	0.7205
	45°	0.7717
	90°	0.8035

a lubricating agent within the ambience. Additionally, the roughness of the friction surface decreases due to heating. After this stage, the fluctuation of the curve and shear strength gradually decrease, and these conditions can also prevent plastic deformation. Therefore, both the coefficient of friction and, consequently, the wear rate exhibit a decrease. Wang et al. [54] reported that the oxide layer formed on the worn surface of the CoCrFeMnNi alloy plays a significant role in lubrication, reducing the coefficient of friction and wear rate under the influence of the applied load. Nagarjuna et al. [55] stated that lower surface roughness causes a decrease in COF, while higher surface roughness causes an increase in COF. As a consequence, the specimen fabricated with a 0° build orientation, characterized by the highest relative density and surface hardness, demonstrated the lowest coefficient of friction (COF) value.

The graphical representation illustrating the wear rate values of the specimens fabricated at various build orientations is provided in Fig. 18. It is observed that as the build orientation of the samples increases, the wear rates also increase. Notably, the specimen fabricated with a 0° build orientation, which exhibited the highest relative density and the lowest coefficient of friction, also achieved the lowest wear rate. The microhardness values of the specimens produced at various build orientations were very close to each other and no major differences were observed. Average hardness values were obtained as 201.2 HV_{0.1} for 0° build orientation, 200 HV_{0.1} for 45° build orientation and 195.8 HV_{0.1} for 90° build orientation, respectively. In a study conducted in the literature, [31] obtained a hardness value of 212 HV₁ for the CoCrFeMnNi alloy produced by the laser powder bed fusion (LPBF) method. In SLM production processes where different structure orientations are used, as the structure orientation angles increase, the number of layers in production also increases and the cooling stages of the layers change accordingly. The hardness of the specimens produced by SLM with 45° and 90° build orientation angles exhibited a decrease with an increase in the number of layers compared to those with a 0° orientation.

The SEM images of wear traces and optical profilometer images of specimens produced in three different build orientations using the optimum parameter set are provided in Fig. 19. Specimens produced with a 0° structure orientation

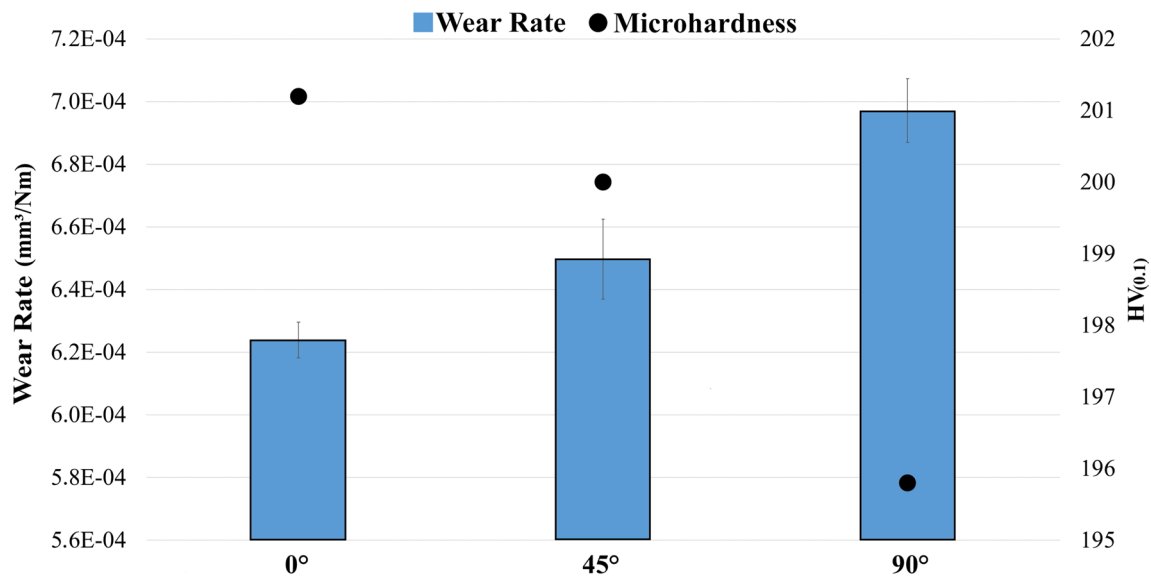


Fig. 18 Microhardness and wear rate graphs of CoCrFeMnNi specimens produced at different build orientations

exhibited lower wear track width and depth compared to specimens produced with other structure orientations. The width of the wear traces increased corresponding to the elevation in build orientation. The continuous accumulation of residues formed during the test causes uneven wear areas due to the wear surface breaking, adhering to the sample, or moving away from the environment [54]. In the sample produced with a 90° construction orientation, ensuring a more balanced contact between the protrusions and the ball resulted in the formation of deeper pits. The cross-sectional width of the samples is close to each other, but the depth of the 0° construction sample is lower than the other samples.

The wear mechanism observed in all samples produced via SLM was evaluated to involve a complex interaction comprising abrasive wear, adhesive wear, and plastic deformation mechanisms. The interaction between the alloy and the abrasive material (Al_2O_3) led to adhesion resulting in the generation of debris in the following stages of the wear test. This situation is especially evident on the surfaces of the 0° and 45°-built specimens. It is understood that the sample surfaces produced in the 0° and 45° construction directions exhibit oxidation reactions due to heating caused by friction under ambient conditions. It reveals abrasive wear, where more scraping occurs on the surfaces of the 90° build sample. Grooves are thought to mostly result from rubbing as a result of contact with each other during friction experiments. The formation of wear couples, along with the debris between them, induces three-body wear, contributing to an increased amount of wear and involving the abrasive wear mechanism in the process, thereby perpetuating the cycle of wear and degradation. This situation was evident in the conspicuous formation of abrasive grooves in the 90°

build sample. This situation is indicative of the formation of oxides and debris particles on the sample surface, which break and become trapped between surfaces, leading to a decrease in wear resistance and thus an increase in the rate of wear. Joseph et al. [56] reported that many deep grooved scratches parallel to the sliding direction appeared on the worn surfaces of the CoCrFeMnNi structure at room temperature, and the wear mechanism of this was abrasive wear.

As a result, the main wear mechanisms of the 0° and 45° build samples are adhesive wear and oxidation wear. Abrasive wear was more common in 90°-build samples. Furthermore, on all sample surfaces, the pile-ups observed at the periphery of the wear traces were indicative of plastic deformation. Considering the surfaces upon which the tribological tests were applied for all distinct build specimens, the 0° build orientation emerged as the most optimum orientation in regards to wear resistance.

3.6 Corrosion Behavior of CoCrFeMnNi Specimens Produced with Different Build Orientations

The open circuit potential (OCP) curves of the specimens produced at three different build orientations using the optimum parameter set are given in Fig. 20. The OCP curves of the 0° and 90° build specimens gradually shifted in the 3.5% NaCl solution towards anodic or toward positive potential values, and they showed an increasing trend as passivation continued. This was an indication that a passive film formed earlier, especially on the 0° and 90° build specimen surfaces. The 0° and 90° build specimens showed numerous small spikes in the open circuit potential. This is an indication of passive film formation followed by degradation and

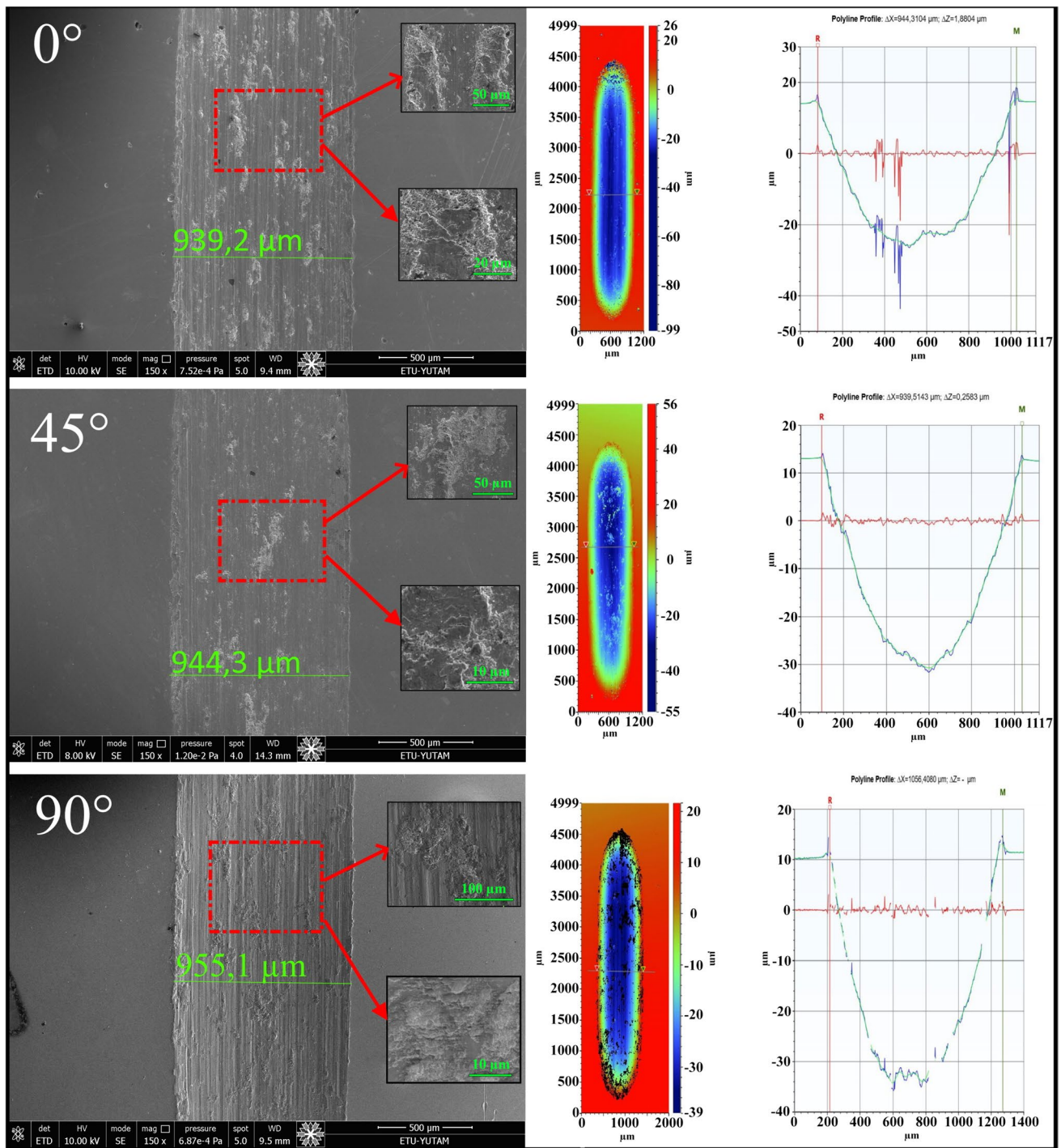


Fig. 19 SEM and 3D-profilometer images of the wear traces of CoCrFeMnNi specimens produced at various build orientations (0°–45°–90°)

re-passivation. As a result, the OCP curves of the specimens obtained with both build orientations were more stable and closely balanced. In the 45° build specimen, OCP values did not exhibit a steady state during the experiment, with many small spikes at the beginning.

Tafel potentiodynamic polarization curves of CoCrFeMnNi HEA produced with different build orientations in a

3.5 wt% NaCl solution are presented in Fig. 21. According to the theory of electrochemical corrosion, corrosion potential (E_{CORR}) is a thermodynamic parameter, and corrosion current density (I_{CORR}) is a kinetic parameter [57]. The corrosion potential signifies the electrochemical potential of a material when it is in an open circuit condition, while the corrosion current density is utilizable for determining the corrosion

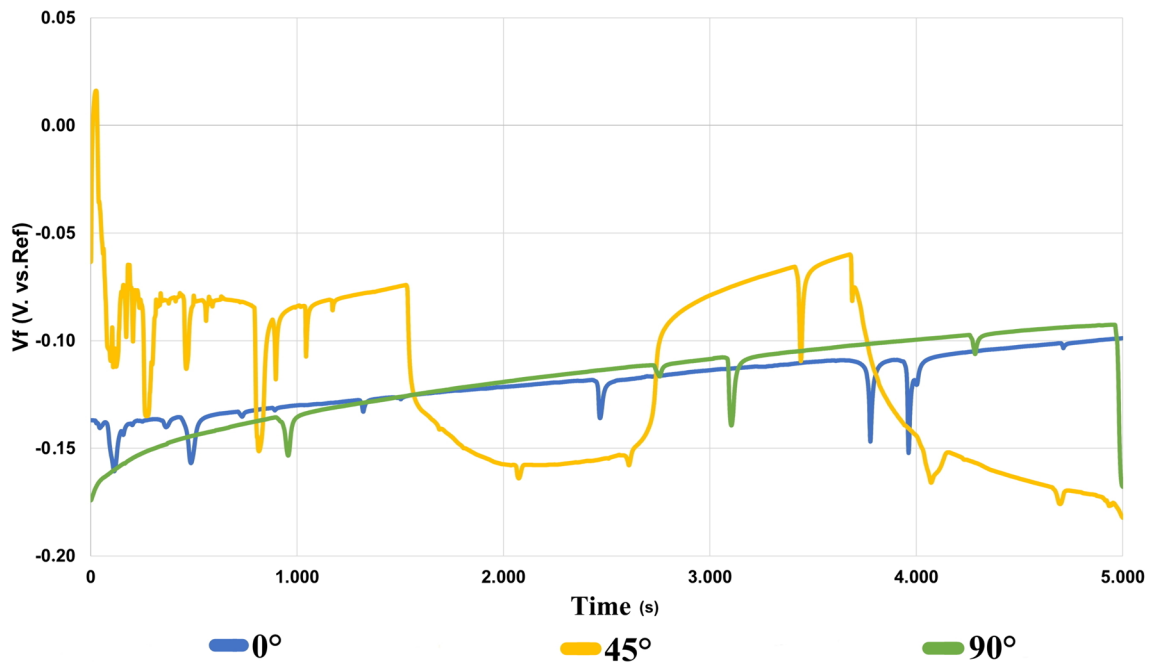


Fig. 20 OCP curves of CoCrFeMnNi specimens produced at different build orientations

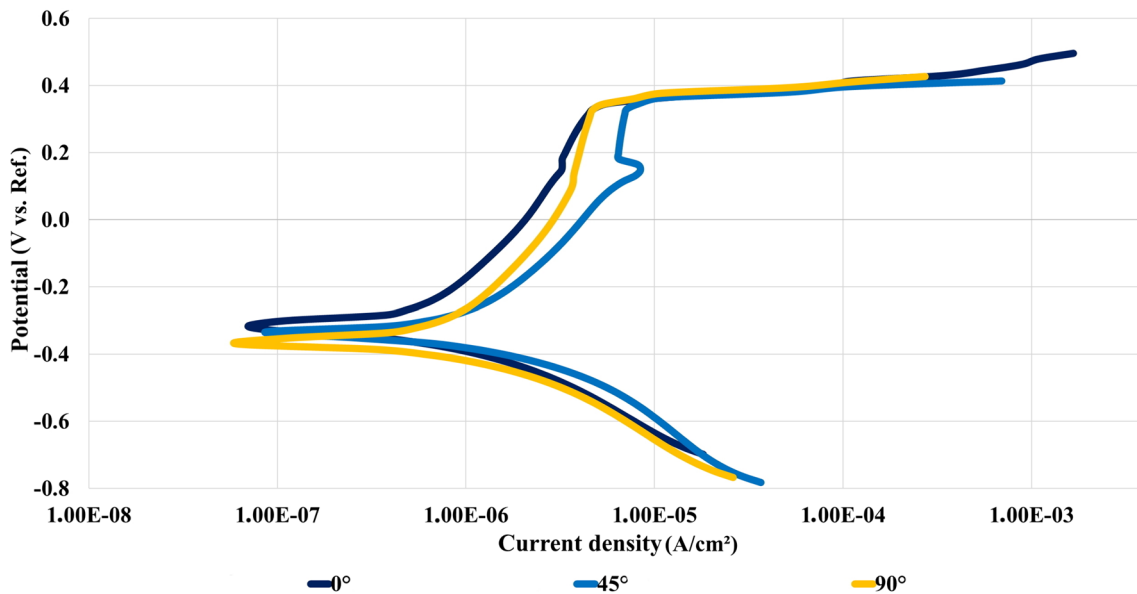


Fig. 21 Potentiodynamic polarization curves of samples produced in different structure orientations

rate of metals. The corrosion rate decreases as the corrosion current density decreases, resulting in improved corrosion resistance. The potential at the dip of curves represents the corrosion potential [33, 58]. When the potentiodynamic polarization curves presented in Fig. 20 were analyzed, it was observed that specimens produced with all three build orientations exhibited typical active–passive potential

behavior. The curves showed significant passive behavior in the anodic region above the E_{corr} values. Under ambient conditions, I_{corr} values were low, and this result showed that the specimens had corrosion resistance in a chloride environment. Although the E_{corr} and I_{corr} values were close to each other for all specimens, specimens produced with a 0° build orientation exhibited higher E_{corr} and lower I_{corr} values

Table 6 Potentiodynamic polarization test results of CoCrFeMnNi specimens produced at different build orientations

Build orientation	E_{corr} (mV)	I_{corr} ($\mu\text{A}/\text{cm}^2$)	Corrosion rate (mpy)
0°	−321	0.883	0.7875
45°	−338	0.2350	2.092
90°	−364	1.480	1.323

(Table 6). The corrosion rate measured at 0.7875 mpy for the 0° build specimen shows a lower value compared to the corrosion rates of the 45° (2.092 mpy) and 90° (1.323 mpy) build specimens. Ren et al. [59] reported that SLM samples with higher density demonstrated superior corrosion resistance compared to cast samples. The reason why the sample produced with a 0° orientation has better corrosion resistance compared to other samples is thought to be due to its higher density and the formation of a more stable passive film on the sample surface. The good corrosion resistance of the CoCrFeMnNi structure is attributed to the elements Co, Cr, and Ni, which can easily form a protective film on the alloy surface [58, 60]. On the other hand, the sample produced with a 45° orientation exhibited lower corrosion resistance, especially due to the overlap of layers in the form of stairs, low density, and high porosity. In addition, the main factor affecting the corrosion rate compared to the corrosion potential is the corrosion current density [57]. Therefore, the highest corrosion current density was found in the sample obtained with a 45° orientation, and as a result, it was the sample with the highest corrosion rate. As a result, it was determined that the samples produced with a 0° build orientation exhibited higher corrosion resistance than those produced with other build orientations.

4 Conclusions

In this study, SLM production parameters were systematically examined in detail, aiming at material and time savings for parts produced from pre-alloyed CoCrFeMnNi HEA powder material. After determining the optimum SLM parameters, their effects on the structural, tribological, mechanical, and corrosion properties of samples produced in different build directions (0°–45°–90°) were discussed comparatively. The main conclusions were summarized as follows:

- The sample produced at 100 W laser power, 600 mm/s scanning speed, 25 μm layer thickness and 70% hatch spacing exhibited ultimate tensile strength of 550 MPa, elongation of 48% and relative density of 99.94%.

- The structure of CoCrFeMnNi powder and the prismatic samples produced with different structures consisted of a single FCC phase and all elements exhibited a homogeneous distribution.
- While the samples produced with 0° structure orientation exhibited a predominantly cellular microstructure, it was observed that the preferential growth of grains and dendritic growth intensified as the structure orientation angle increased.
- The samples produced with a 0° build orientation exhibited the lowest wear track width and depth ratios and demonstrated the lowest wear rate.
- Average hardness values were obtained as 201.2 $\text{HV}_{0.1}$ for 0° build orientation, 200 $\text{HV}_{0.1}$ for 45° build orientation, and 195.8 $\text{HV}_{0.1}$ for 90° build orientation, respectively.
- In 3.5% NaCl solution, the 0° build sample exhibited better corrosion resistance compared to the 45° (2.092) and 90° (1.323 mpy) build samples, with a corrosion rate of 0.7875 mpy.

Funding Open access funding provided by the Scientific and Technological Research Council of Türkiye (TÜBİTAK). Türkiye Bilimsel ve Teknolojik Araştırma Kurumu, 122M679, Caner Bulut.

Declarations

Conflict of interest All the authors declare that they have no known competing financial interests or personal relationships that could have appeared to influence the work reported in this paper. All the authors declare the following financial interests/personal relationships which may be considered as potential competing interests.

Open Access This article is licensed under a Creative Commons Attribution 4.0 International License, which permits use, sharing, adaptation, distribution and reproduction in any medium or format, as long as you give appropriate credit to the original author(s) and the source, provide a link to the Creative Commons licence, and indicate if changes were made. The images or other third party material in this article are included in the article's Creative Commons licence, unless indicated otherwise in a credit line to the material. If material is not included in the article's Creative Commons licence and your intended use is not permitted by statutory regulation or exceeds the permitted use, you will need to obtain permission directly from the copyright holder. To view a copy of this licence, visit <http://creativecommons.org/licenses/by/4.0/>.

References

1. J.W. Yeh, S.K. Chen, S.J. Lin, J.Y. Gan, T.S. Chin, T.T. Shun, C.H. Tsau, S.Y. Chang, *Adv. Eng. Mater.* **6**(5), 299–303 (2004). <https://doi.org/10.1002/adem.200300567>
2. B. Cantor, I.T.H. Chang, P. Knight, A.J.B. Vincent, *Mater. Sci. Eng. A* **375–377**, 213–218 (2004). <https://doi.org/10.1016/j.msea.2003.10.257>

3. J.P. Oliveira, A. Shamsolhodaei, J. Shen, J.G. Lopes, R.M. Gonçalves, M. de Brito Ferraz, L. Piçarra, Z. Zeng, N. Schell, N. Zhou, H.S. Kim, *Mater. Des.* **219**, 110717 (2022). <https://doi.org/10.1016/j.matdes.2022.110717>
4. J.W. Yeh, *Ann. Chim. Sci. Des Mater.* **31**(6), 633–648 (2006). <https://doi.org/10.3166/acsm.31.633-648>
5. X.Y. Gu, Y.N. Dong, Y.X. Zhuang, J. Wang, *Met. Mater. Int.* **26**, 292–301 (2020). <https://doi.org/10.1007/s12540-019-00328-w>
6. M.J. Jang, S.H. Joo, C.W. Tsai, J.W. Yeh, H.S. Kim, *Met. Mater. Int.* **22**, 982–986 (2016). <https://doi.org/10.1007/s12540-016-6304-2>
7. C. Bulut, F. Yıldız, T. Varol, S.B. Akçay, T.O. Ergüder, *High Temp. Corros. Mater.* **101**, 225–249 (2024). <https://doi.org/10.1007/s11085-023-10213-y>
8. D. Yang, Y. Liu, H. Jiang, M. Liao, N. Qu, T. Han, Z. Lai, J. Zhu, *J. Alloys Compd.* **823**, 153729 (2020). <https://doi.org/10.1016/j.jallcom.2020.153729>
9. Y. Chen, W. Liu, H. Wang, J. Xie, T. Zhang, L. Yin, Y. Huang, *Entropy* **24**(2), 241 (2022). <https://doi.org/10.3390/e24020241>
10. J.P. Oliveira, T.M. Curado, Z. Zeng, J.G. Lopes, E. Rossinyol, J.M. Park, N. Schell, F.M. Braz Fernandes, H.S. Kim, *Mater. Des.* **189**, 108505 (2020). <https://doi.org/10.1016/j.matdes.2020.108505>
11. Y.K. Kim, M.C. Kim, K.A. Lee, *J. Mater. Sci. Technol.* **97**, 10–19 (2022). <https://doi.org/10.1016/j.jmst.2021.04.030>
12. E.S. Kim, K.R. Ramkumar, G.M. Karthik, S.G. Jeong, S.Y. Ahn, P. Sathiyamoorthi, H. Park, Y.U. Heo, H.S. Kim, *J. Alloys Compd.* **942**, 169062 (2023). <https://doi.org/10.1016/j.jallcom.2023.169062>
13. Y. Ren, L. Liang, Q. Shan, A. Cai, J. Du, Q. Huang, S. Liu, X. Yang, Y. Tian, H. Wu, *Virtual Phys. Prototyp.* **15**, 543–554 (2020). <https://doi.org/10.1080/17452759.2020.1848284>
14. Y.K. Kim, J.H. Yu, H.S. Kim, K.A. Lee, *Compos. Part B Eng.* **210**, 108638 (2021). <https://doi.org/10.1016/j.compositesb.2021.108638>
15. F. Wang, T. Yuan, R. Li, S. Lin, P. Niu, V. Cristino, *Int. J. Refract. Met. Hard Mater.* **111**, 106107 (2023). <https://doi.org/10.1016/j.jrmhm.2023.106107>
16. L. Thijs, F. Verhaeghe, T. Craeghs, J. Van Humbeeck, J.P. Kruth, *Acta Mater.* **58**(9), 3303–3312 (2010). <https://doi.org/10.1016/j.actamat.2010.02.004>
17. C. Kusuma, S.H. Ahmed, A. Mian, R. Srinivasan, *J. Mater. Eng. Perform.* **26**, 3560–3568 (2017). <https://doi.org/10.1007/s11665-017-2768-6>
18. I. Yadroitsev, P. Bertrand, I. Smurov, *Appl. Surf. Sci.* **253**(19), 8064–8069 (2007). <https://doi.org/10.1016/j.apsusc.2007.02.088>
19. I. Hacısalıhoğlu, F. Yıldız, A. Çelik, *Mater. Sci. Eng. A* **802**, 140649 (2021). <https://doi.org/10.1016/j.msea.2020.140649>
20. J.P. Oliveira, A.D. LaLonde, J. Ma, *Mater. Des.* **193**, 108762 (2020). <https://doi.org/10.1016/j.matdes.2020.108762>
21. A.M. Mancisidor, F. Garcıandia, M.S. Sebastian, P. Álvarez, J. Díaz, I. Unanue, *Phys. Procedia* **83**, 864–873 (2016). <https://doi.org/10.1016/j.phpro.2016.08.090>
22. R. Li, J. Liu, Y. Shi, L. Wang, W. Jiang, *Int. J. Adv. Manuf. Technol.* **59**, 1025–1035 (2012). <https://doi.org/10.1007/s00170-011-3566-1>
23. J.M. Park, J. Choe, J.G. Kim, J.W. Bae, J. Moon, S. Yang, K.T. Kim, J.H. Yu, H.S. Kim, *Mater. Res. Lett.* **8**(1), 1–7 (2020). <https://doi.org/10.1080/21663831.2019.1638844>
24. W. Wu, R. Zhou, B. Wei, S. Ni, Y. Liu, M. Song, *Mater. Charact.* **144**, 605–610 (2018). <https://doi.org/10.1016/j.matchar.2018.08.019>
25. Q. Ye, K. Feng, Z. Li, F. Lu, R. Li, J. Huang, Y. Wu, *Appl. Surf. Sci.* **396**, 1420–1426 (2017). <https://doi.org/10.1016/j.apsusc.2016.11.176>
26. Y. Kim, J. Choe, K. Lee, *J. Alloys Compd.* **805**, 680–691 (2019). <https://doi.org/10.1016/j.jallcom.2019.07.106>
27. J. Zhang, Y. Yan, B. Li, *Materials (Basel)*. **15**(23), 8560 (2022). <https://doi.org/10.3390/ma15238560>
28. C. Zhang, K. Feng, H. Kokawa, Z. Li, *Mater. Charact.* **196**, 112586 (2023). <https://doi.org/10.1016/j.matchar.2022.112586>
29. X. Jia, Z. Xu, Y. He, S. Zhou, X. Du, H. Zhang, A. Mao, *Met. Mater. Int.* **29**(10), 2895–2908 (2023). <https://doi.org/10.1007/s12540-023-01415-9>
30. R. Li, P. Niu, T. Yuan, P. Cao, C. Chen, K. Zhou, *J. Alloys Compd.* **746**, 125–134 (2018). <https://doi.org/10.1016/j.jallcom.2018.02.298>
31. A. Pigionio, B. Dovggy, C. Liu, C.M. Gourlay, P.A. Hooper, M.S. Pham, *Mater. Lett.* **224**, 22–25 (2018). <https://doi.org/10.1016/j.matlet.2018.04.052>
32. Z.G. Zhu, Q.B. Nguyen, F.L. Ng, X.H. An, X.Z. Liao, P.K. Liaw, S.M.L. Nai, J. Wei, *Scr. Mater.* **154**, 20–24 (2018). <https://doi.org/10.1016/j.scriptamat.2018.05.015>
33. R. Savinov, J. Shi, *Mater. Sci. Addit. Manuf.* **2**(1), 42 (2023). <https://doi.org/10.36922/msam.42>
34. N. Li, S. Wu, D. Ouyang, J. Zhang, L. Liu, *J. Alloys Compd.* **822**, 153695 (2020). <https://doi.org/10.1016/j.jallcom.2020.153695>
35. J. Karimi, L. Kollo, R. Rahmani, P. Ma, Y.D. Jia, K.G. Prashanth, *J. Manuf. Process.* **84**, 55–63 (2022). <https://doi.org/10.1016/j.jmpro.2022.09.056>
36. C. Zhang, K. Feng, H. Kokawa, B. Han, Z. Li, *Mater. Sci. Eng. A* **789**, 139672 (2020). <https://doi.org/10.1016/j.msea.2020.139672>
37. A. Kumar, M. Arvind, *Lasers Manuf. Mater. Process.* (2024). <https://doi.org/10.1007/s40516-023-00243-4>
38. J. Yoshioka, M. Eshraghi, *Heat Mass Transfer* **59**(9), 1155–1166 (2023). <https://doi.org/10.1007/s00231-022-03318-8>
39. W. Yuan, H. Chen, T. Cheng, Q. Wei, *Mater. Des.* **189**, 108542 (2020). <https://doi.org/10.1016/j.matdes.2020.108542>
40. U. Gençoğlu, G. Kaya, T.O. Ergüder, İ. Hacısalıhoğlu, F. Yıldız, *J. Mater. Eng. Perform.* **31**(5), 3688–3703 (2022). <https://doi.org/10.1007/s11665-021-06507-4>
41. M. Sun, B. Wang, J. Zhang, B. Lu, *Intermetallics* **156**, 107866 (2023). <https://doi.org/10.1016/j.intermet.2023.107866>
42. A.K. Dutt, G.K. Bansal, S. Tripathy, K. Gopala Krishna, V.C. Srivastava, S. Ghosh Chowdhury, *Trans. Indian Inst. Met.* **76**(2), 335–345 (2023). <https://doi.org/10.1007/s12666-022-02687-2>
43. M. Zamani, H. Mirzadeh, H.M. Ghasemi, *Mater. Res. Express* **5**(6), 066548 (2018). <https://doi.org/10.1088/2053-1591/aacd96>
44. A.J. Pirlari, M. Emamy, A.A. Amadeh, M. Naghizadeh, *J. Mater. Eng. Perform.* **28**, 6912–6920 (2019). <https://doi.org/10.1007/s11665-019-04403-6>
45. M. Naghizadeh, H. Mirzadeh, *Steel Res. Int.* **90**(10), 1900153 (2019). <https://doi.org/10.1002/srin.201900153>
46. Q. Sun, D. Du, L. He, A. Dong, C. Zhang, B. Sun, *J. Alloys Compd.* **938**, 168562 (2023). <https://doi.org/10.1016/j.jallcom.2022.168562>
47. Y. Chew, G.J. Bi, Z.G. Zhu, F.L. Ng, F. Weng, S.B. Liu, S.M.L. Nai, B.Y. Lee, *Mater. Sci. Eng. A* **744**, 137–144 (2019). <https://doi.org/10.1016/j.msea.2018.12.005>
48. J. Song, Y. Chew, G. Bi, X. Yao, B. Zhang, J. Bai, S.K. Moon, *Mater. Des.* **137**, 286–297 (2018). <https://doi.org/10.1016/j.matdes.2017.10.033>
49. W. Shifeng, L. Shuai, W. Qingsong, C. Yan, Z. Sheng, S. Yusheng, *J. Mater. Process. Technol.* **214**(11), 2660–2667 (2014). <https://doi.org/10.1016/j.jmatprotec.2014.06.002>
50. P. Ji, Y. Jia, P. Ma, Y. Mu, K. Sun, G. Wang, *J. Mater. Res. Technol.* **23**, 3166–3176 (2023). <https://doi.org/10.1016/j.jmrt.2023.01.219>
51. R. Savinov, Y. Wang, J. Wang, J. Shi, *Procedia Manuf.* **53**, 435–442 (2021). <https://doi.org/10.1016/j.promfg.2021.06.046>

52. Z. Tong, X. Pan, W. Zhou, Y. Yang, Y.X. Ye, D. Qian, X. Ren, *Surf. Coat. Technol.* **422**, 127504 (2021). <https://doi.org/10.1016/j.surfcoat.2021.127504>
53. H.T. Wang, H.L. Yao, M.X. Zhang, X.B. Bai, Z.H. Yi, Q.Y. Chen, G.C. Ji, *Surf. Coat. Technol.* **374**, 485–492 (2019). <https://doi.org/10.1016/j.surfcoat.2019.04.093>
54. Y. Wang, D. Li, J. Yang, J. Jin, M. Zhang, X. Wang, B. Li, Z. Hu, P. Gong, *Materials (Basel)* **16**(4), 1714 (2023). <https://doi.org/10.3390/ma16041714>
55. C. Nagarjuna, A. Sharma, K. Lee, S.-J. Hong, B. Ahn, J. Mater. Res. Technol. **22**, 1708–1722 (2023). <https://doi.org/10.1016/j.jmrt.2022.12.070>
56. J. Joseph, N. Haghdadadi, K. Shamlaye, P. Hodgson, M. Barnett, D. Fabijanic, *Wear* **428–429**, 32–44 (2019). <https://doi.org/10.1016/j.wear.2019.03.002>
57. H. Peng, Z. Lin, R. Li, P. Niu, Z. Zhang, *Front. Mater.* **7**, 244 (2020). <https://doi.org/10.3389/fmats.2020.00244>
58. X. Jin, X. Gu, F. Quan, X. Ran, K. Zhang, A. Mao, *Materwiss. Werksttech.* **50**(7), 837–843 (2019). <https://doi.org/10.1002/mawe.201800095>
59. J. Ren, C. Mahajan, L. Liu, D. Follette, W. Chen, S. Mukherjee, *Metals (Basel)* **9**(10), 1029 (2019). <https://doi.org/10.3390/met9101029>
60. C. Shang, E. Axinte, J. Sun, X. Li, P. Li, J. Du, P. Qiao, Y. Wang, *Mater. Des.* **117**, 193–202 (2017). <https://doi.org/10.1016/j.matdes.2016.12.076>

Publisher's Note Springer Nature remains neutral with regard to jurisdictional claims in published maps and institutional affiliations.